Very high cycle fatigue characteristics of laser beam powder bed fused AlSi10Mg: A systematic evaluation of part geometry

International Journal of Fatigue 189 (2024) 108544

Contents lists available at ScienceDirect

International Journal of Fatigue

journal homepage: www.elsevier.com/locate/ijfatigue

Very high cycle fatigue characteristics of laser beam powder bed fused AlSi10Mg: A systematic evaluation of part geometry

Kamin Tahmasbi [a], Muztahid Muhammad [b,c], Maryam Avateffazeli [a], Mohammadreza Yaghoobi [d], Andrea Tridello [e], Davide S. Paolino [e], Shuai Shao [b,c], Nima Shamsaei [b,c], Meysam Haghshenas [a,*]

[a] Fatigue, Fracture, and Failure Laboratory (F3L), Department of Mechanical, Industrial, and Manufacturing Engineering (MIME), the University of Toledo, OH 43606, USA
[b] Department of Mechanical Engineering, Auburn University, Auburn, AL 36849, USA
[c] National Center for Additive Manufacturing Excellence, Auburn University, Auburn, AL 36849, USA
[d] Materials Science and Engineering, University of Michigan, Ann Arbor, MI 48109, USA
[e] Department of Mechanical and Aerospace Engineering, Politecnico di Torino, 10129 Turin, Italy

ARTICLE INFO

Keywords:
Very high cycle fatigue
Laser beam powder bed fusion
AlSi10Mg
Ultrasonic Fatigue
Part geometry

ABSTRACT

This study explores the influence of geometry and part size on defect distribution, melt pool size, and mechanical characteristics in laser beam powder bed fused (LB-PBF) AlSi10Mg. Five distinct geometries—hourglass, small rod, small block, large block, and large rod—were fabricated under identical process parameters. Fully reversed ultrasonic fatigue testing, operating at a frequency of 20 kHz, was conducted to assess the very high cycle fatigue properties. The findings indicated that part geometry had a major impact on the fatigue properties of the material in the very high cycle fatigue regime. Specimens machined from large rods and large blocks had the lowest porosity and highest fatigue resistance. Microstructural analysis indicated that hourglass, small rod, and small block specimens had shallower melt pools and overlap depths compared to other geometries. This observation suggests a higher cooling rate in specimens with smaller cross-sectional areas, leading to the increased presence of entrapped gas pores and a lack of fusion defects. Understanding the relationship between part geometry and fatigue properties in LB-PBF components offers insights for optimizing design and manufacturing processes in additive manufacturing applications.

1. Introduction

The current focus on additive manufacturing (AM) of metallic alloys, particularly Al-Si alloys, has garnered significant attention due to its pivotal role in the design and fabrication of complex structural components across aerospace, military, and automotive industries. AM technologies, such as laser beam powder bed fusion (LB-PBF), enable the production of lightweight structures with intricate geometries that were previously impractical using conventional manufacturing methods [1,2]. Nevertheless, volumetric flaws like a lack of fusion (LoF), keyholes, and entrapped gas holes are unavoidable at this stage of laser beam powder bed fusion (LB-PBF) technology. The thermal conditions encountered during manufacturing, influenced by both process parameters (i.e., laser power, scanning speed, layer thickness, and hatch spacing) and design parameters (such as part geometry and build orientation), could affect the characteristics of defects, including their size, location, and quantity [3–7]. Understanding how design parameters such as part geometry, size, build orientation, and inter-layer time intermissions affect the distribution and occurrence of volumetric defects is crucial for certifying and qualifying LB-PBF materials and parts. This is essential because the presence of these defects reduces the fatigue strength of LB-PBF parts relative to their wrought (or cast) equivalents [8–11].

The build orientation [3,12–17] and inter-layer time intervals [18–20] are the factors that have been studied for assessing the effect of additive manufacturing design parameters on the volumetric defects' features, as well as the mechanical properties that arise. Xu et al. [12,13] conducted a thorough investigation into the impact of build orientation on the very high cycle fatigue (VHCF) performance of LB-PBF AlSi10Mg specimens and discovered a substantial relationship between fatigue

* Corresponding author.
E-mail address: meysam.haghshenas@utoledo.edu (M. Haghshenas).

https://doi.org/10.1016/j.ijfatigue.2024.108544
Received 21 April 2024; Received in revised form 14 July 2024; Accepted 8 August 2024
Available online 12 August 2024

performance and specimen build orientation. They discovered a maximum fatigue limit of around 110 MPa for the horizontally built samples owing to the lower defect size in the horizontally produced specimens while the 45° and 90° samples exhibit a comparable fatigue limit of about 87 MPa at 10^8 cycles [13].

Comparable findings were reported for LB-PBF AlSi10Mg [3,14,16,21,22], where it was observed that the horizontally built specimens exhibited significantly better fatigue performance than the vertically built specimens. This is attributed to the larger defect size and orientation of the flat pores, which were perpendicular to the loading direction in the vertically built specimens [16,22]. The authors also noted that there is a considerable scatter in the number of cycles until failure, with the minimum scatter observed in the horizontally built samples [14,21]. On the other hand, Gerov et al. [23] found decreased fatigue life for the horizontally built specimens compared to the vertically built specimens. The vertically built specimens also showed better fatigue performance, according to Piette et al. [11]. They found a "halo" surrounding internal LoF defects in all vertically built specimens that were absent in all horizontally built specimens [11]. There were two different fracture mechanisms seen in the "halo," and they resembled fish-eye initiation sites seen in high-strength steels subject to the VHCF regime [11]. This might be the cause of the vertically built specimens' superior fatigue performance over the horizontally built specimens.

Additionally, variations in heat dissipation during the printing of a part and changes in the creation of defects like surface roughness and porosity can be caused by the orientation at which the specimens are manufactured. Pegues et al. [24] reported that the surface roughness was higher for the down-skin surface (i.e., the surface facing the build plate) than for the up-skin surface (i.e., the surface facing opposite to the build plate) in specimens of LB-PBF Ti-6Al-4 V produced at a 45-degree angle relative to the built plate (referred to as the diagonal direction). The variation in the amount of solidified material accessible for thermal dissipation throughout the manufacturing process of up-skin and down-skin surfaces was ascribed to the variance in surface roughness. Heat dissipation was mostly via the previously solidified layers during the creation of up-skin surfaces. However, the surface of the specimen remained at elevated temperatures for an extended duration during the manufacture of downward-facing skin surfaces, primarily because of the reduced level of solidified material presented for dissipating heat. Consequently, this situation may result in a greater accumulation of incompletely melted powder grains adhering to the surface, thereby augmenting surface roughness. All specimens had cracks that started on the down-skin surface, which had the roughest surface. Moreover, it was shown by AM modeling that raising the inter-layer time interval results in lower peak temperatures and faster cooling rates [25,26]. The resulting deviations in thermal history can impact microstructures and defect content. For instance, Mahmoudi et al. [27] studied the effects of inter-layer time intervals on the uniaxial tensile and compressive characteristics of LB-PBF 17–4 PH SS. They reported a variation in hardness that was related to the variances in the microstructure seen because of variations in the thermal history. A lower cooling rate and higher bulk temperature during the manufacturing of single-built specimens caused residual austenite to exist, which lowered the hardness of LB-PBF 17–4 PH SS specimens.

It was observed that the geometry of the fatigue test coupon significantly impacts high cycle fatigue (HCF) and VHCF performance of LB-PBF specimens. Tridello et al. [28] examined how the risk volume of the LB-PBF AlSi10Mg laboratory sample affected VHCF performance. They utilized an hourglass specimen (250 mm^3 risk volume) and a Gaussian specimen (2330 mm^3 risk volume) and found that increasing the risk volume of the final ultrasonic fatigue testing sample leads to reduced fatigue life due to the larger defect size [28]. According to Paolino et al. [29], increasing risk volume might result in more scattered fatigue findings for LB-PBF AlSi10Mg samples. However, there is no study in the literature about the impacts of AM part geometry on the thermal history and defect distribution of the LB-PBF Al-Si part. Few research investigations have been done on the effects of part geometry and size on the thermal history, defects, and fatigue behavior of other alloys. During the AM process, it has been demonstrated that the thermal history experienced by parts with various geometries or even at discrete positions within a part can vary. Shrestha et al. [30] investigated how part size and geometry affected the melt pool size, microstructural characteristics, and resultant mechanical characteristics of LB-PBF 17–4 PH SS. A small impact of part geometry on the tensile performance of the LB-PBF 17–4 PH SS was proven by experimental data, while part geometry had a substantial influence on fatigue performance in the high cycle fatigue regime. The lowest porosity was found in specimens made from large square blocks, which also had the maximum fatigue resistance. In contrast, the specimens made from dog bone specimens had the highest level of porosity, which led to a lower fatigue resistance than that of other geometries. It was also discovered that the melt pool depth was smaller for dog-bone specimens and greater for large block specimens, indicating some impacts of geometry on the melt pool dimensions [30]. Soltani-Tehrani [31] studied the effects of changing scanning speed on the thermal history, defects, microstructure, and fatigue behavior of LB-PBF 17–4 PH SS parts of various geometries. It was observed that lowering the scanning speed during fabrication while increasing input energy within the process window led to deeper melt pools and melt pool overlaps, which in turn led to fewer volumetric defects, notably LoF, in the material. Shanbhag et al. [32] also examined the impact of specimen geometry on the tensile properties of Ti-6Al-4 V fabricated by electron beam powder bed fusion. An increase in yield, tensile strength, and elastic modulus was seen with an increase in the cross-sectional area of specimens. However, the yield and tensile strength decreased as the surface area to volume ratio of specimens increased [32].

Existing studies have demonstrated how design elements like part size and shape may significantly impact the thermal history of the LB-PBF process. This variance in thermal history may result in changes in the characteristics of defects, which in turn may have an impact on the part's fatigue performance. Hence, before these parts may be utilized in uses where they are subject to cyclic loads, it is crucial to understand the impacts of design parameters on the fatigue behavior of AM components. Although there are several research works on the impacts of layer orientation, inter-layer time interval, and part geometry on the fatigue response of materials in low and high-cycle fatigue domains, there has not been a comprehensive analysis of how geometry variations affect the microstructure, defect characteristics, and fatigue performance of LB-PBF components in VHCF domain. To close this gap, this study will investigate how the part geometry and size affect the tensile and VHCF characteristics concerning defect size and distribution. To investigate the VHCF behavior, ultrasonic fatigue (USF) tests have been conducted on LB-PBF AlSi10Mg parts, a widely explored and adopted LB-LBPF aluminum alloy for aerospace and automotive applications [2,33,34], with different geometries. Following the introduction section, the material and methodology section is described, and then the results for fatigue lives of different specimens are presented and discussed drawing upon discrepancies in the thermal histories encountered during the LB-PBF process.

2. Experimental procedure

2.1. Material and parts building

In this investigation, AlSi10Mg powder from Carpenter Additive that

Table 1
Chemical composition of AlSi10Mg powder provided by Carpenter Additive.

Element	Al	Si	Mg	Fe	Cu	Ni, Zn, Pb, Sn, Ti, Mn
Weight Percent (Wt.%)	Balance	9.60	0.38	0.18	<0.05	<0.01

was atomized with argon was used. The chemical composition of this material is shown in Table 1 which was obtained from the test certificate provided by the powder supplier, Carpenter Additive. However, the technique to determine the chemical composition was not specified by the powder supplier. It should be mentioned that virgin powder was used for fabricating the parts and all components were produced using the Renishaw (RenAM 500Q), an LB-PBF machine, in the vertical direction (i.e. normal to the build plate), in an argon atmosphere.

Five distinct sets of part geometries, comprising an oversized hourglass part with a 6 mm diameter at the narrowest section (i.e., indicating the laboratory test specimen or the witness coupon), two kinds of square rods with a cross-section of 12 × 12 mm^2 and 25 × 25 mm^2, and two types of cylindrical rods with diameters of 12 mm and 35.36 mm, as illustrated in Fig. 1, respectively, were made. These parts were created to introduce changes in thermal history due to variances in part size and geometry. It is important to note that specimens from each batch were randomly distributed all over the build platform and due to the absence of a thermal imaging system in the Renishaw machine, the heat distribution across the entire build plate could not be assessed. Neighboring effects were not considered, as they were outside the scope of this study. All parts were manufactured employing the manufacturer-recommended process parameters, which are listed in Table 2, and the stripe scanning pattern was used for AM. Additionally, one part of each geometry was fabricated up to the midpoint of the gage section (referred to as a half-built sample) to enable precise analysis of melt pool size at the gage section of the specimens.

According to the design depicted in Fig. 2(a), all specimens with five different geometries were machined into equally sized final hourglass specimens (Fig. 2(c)) to decrease the variability in the specimens and be able to run the ultrasonic fatigue tests at 20 kHz frequency. No effect of the contour process parameters on the results of the mechanical tests was expected because all the specimens used in this investigation were machined to sufficient depths. Following machining, every specimen underwent polishing to achieve a mirror finish using a sequence of sandpapers (240 grit to 4000 grit). For convenient reference, the specimens are machined from oversized hourglass parts, square rods with a cross-section of 12 × 12 mm^2, square rods with a cross-section of 25 × 25 mm^2, cylindrical rods with 12 mm diameter and cylindrical rods with 35.36 mm diameter shall all be denoted as hourglass (HG), small block (SB), large block (LB), small rod (SR), and large rod (LR), respectively, throughout this article.

All specimens underwent only a stress relief process after their manufacture, before being separated from the build platform using a wire cut. Therefore, all the samples were held at 300 °C for 2 h inside an electric furnace in an argon atmosphere and then cooled down in the

Table 2
The process parameters managed for the manufacturing of LB-PBF AlSi10Mg specimens in this study.

Laser power (W)	Scanning speed (mm/s)	Hatch spacing (μm)	Layer thickness (μm)	Resulting energy density (J/mm^3)
350	1800	90	30	72

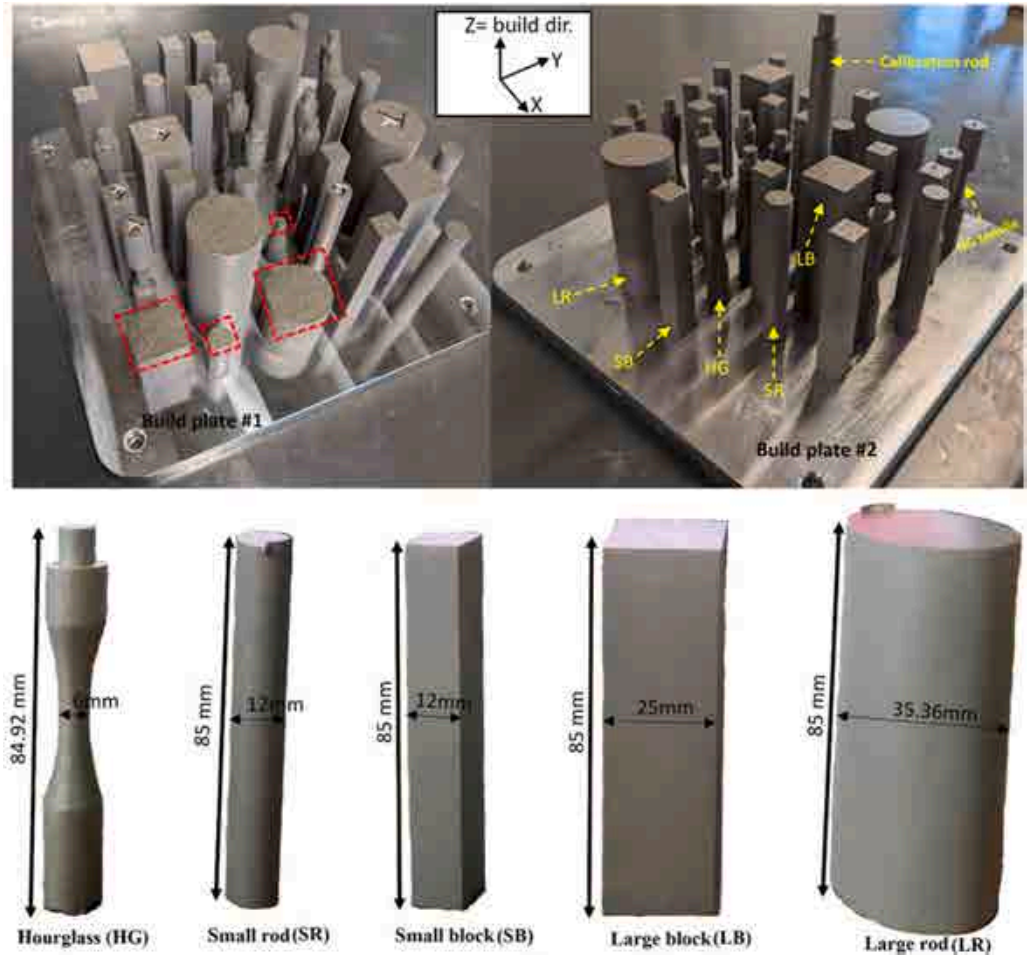

Fig. 1. LB-PBF AlSi10Mg parts printed in the vertical direction with five unique geometries to run ultrasonic fatigue and tensile tests. The half-built melt pool specimens are marked with red dashed boxes in build plate #1. (For interpretation of the references to color in this figure legend, the reader is referred to the web version of this article.)

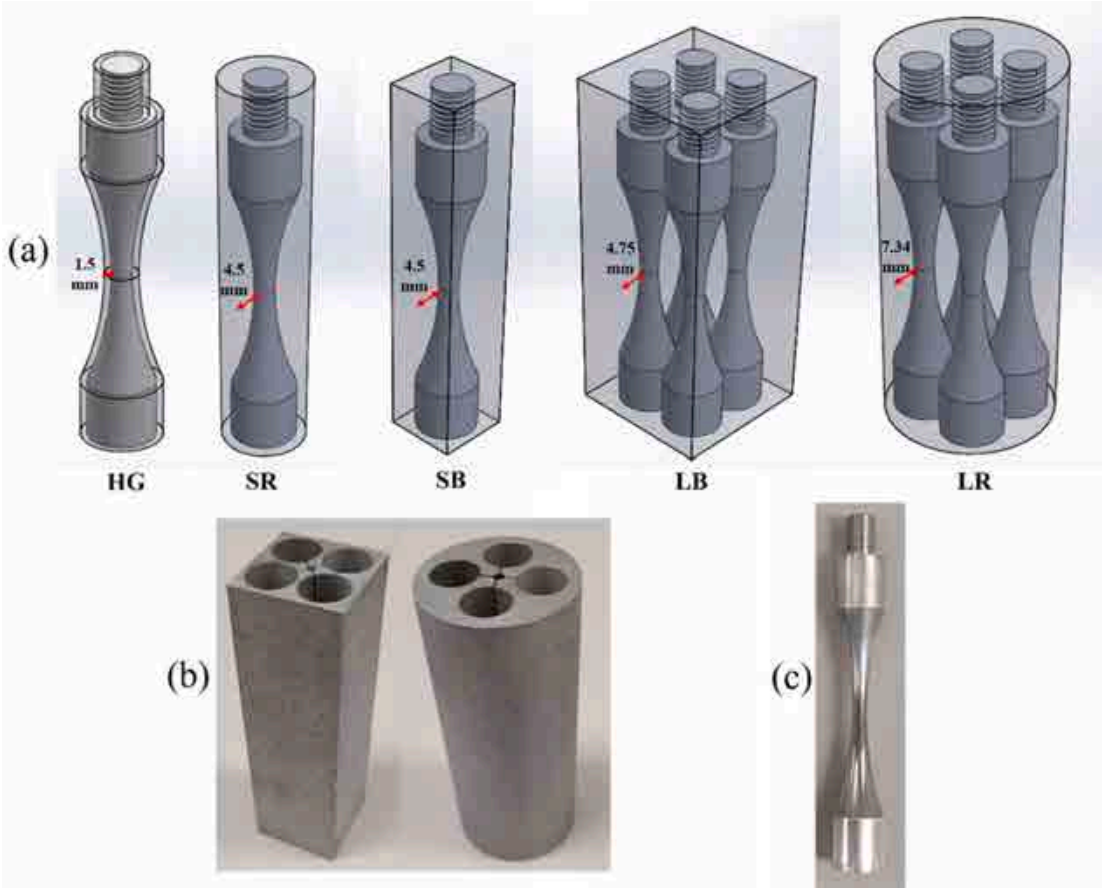

Fig. 2. (a) Schematic drawings of the design used for HG, SR, SB, LB, and LR specimens to show the number and location of final hourglass samples extracted from each part geometry (red marker shows the distance between the outer surface during printing and the final surface of the gage section of fatigue samples for each specimen geometry); (b) LB and LR parts after EDM wire cut to extract specimens; (c) A final hourglass ultrasonic fatigue specimen. (For interpretation of the references to color in this figure legend, the reader is referred to the web version of this article.)

furnace. It is also important to note that the used heat treatment is not anticipated to change the size and distribution of the LB-PBF-induced volumetric defects [35].

2.2. Microstructure analysis and fractography

In this study, microstructure analysis was performed utilizing a Keyence VHX-600 Digital Microscope to explore the impact of part geometry and thermal history on the melt pool characteristics of LB-PBF AlSi10Mg. For the SR, SB, LB, and LR samples, extra care was taken to make sure that, after machining, the melt pool measurements came from the sites that represented the gage section of the ultrasonic fatigue specimens. Melt pools from the new layers might affect the melt pools created in the previously formed layers since melt pool depths are usually larger than layer thicknesses. Melt pool studies were thus performed on the upper layer of the half-built parts. The melt pool attributes, which include depths and overlap depths between consecutive tracks, were measured by cutting samples longitudinally (i.e., parallel to the build direction) in a direction normal to the scan direction of the top layer. The cut samples were then cold-mounted in epoxy. To achieve a mirror-like surface quality, mounted samples were first ground using various reducing grit sandpapers. Subsequently, a polishing stage was performed using colloidal silica.

The mounted and polished half-built samples were chemically etched using Keller's reagent (95 mL water, 2.5 mL HNO_3, 1.5 mL HCl, 1.0 mL HF) to reveal the effect of part geometry on the physical appearance of the melt pool in LB-PBF AlSi10Mg. Furthermore, scanning electron microscopy (SEM) was conducted on the etched longitudinal microsections of each geometry to see whether there was any change in the microstructure and initial silicon network of the specimens with different geometries after manufacturing and stress relief heat treatment.

Following the completion of the ultrasonic fatigue tests, fractography using an SEM was performed to determine the factors that could influence the initiation and propagation of cracks. Before each surface was evaluated, the fracture surfaces were also sonicated in a water-isopropanol solution to eliminate any potential moisture or debris and then the surfaces were cleaned with acetone. All the fractography and SEM microstructural analysis used in this study were captured using a Zeiss Crossbeam 550 SEM.

2.3. Porosity analysis

For the porosity analysis, a volume of ~35 mm^3 from the middle of the gage section of at least one LB-PBF AlSi10Mg hourglass ultrasonic fatigue specimen of each geometry was scanned using a Zeiss Xradia 620 Versa X-ray computed tomography (XCT) machine and the length of the scanned region along the long axis of the specimen was ~5 mm. The scanning was conducted at a source voltage of 60 kV and a power of 6.5 W, with an X-ray filter to reduce low-energy photon counts. A voxel size of approximately 5 μm was maintained in all directions during the X-ray CT scans. Volumetric reconstruction from the acquired projections was performed manually using the proprietary Xradia Versa software and post-processing was performed utilizing ImageJ and Dragonfly software. Defects minor than a 15 μm equivalent diameter were excluded from the analysis to prevent false detection from noise.

2.4. Mechanical and fatigue testing

In this investigation, ultrasonic fatigue testing was performed under fully reversed loading (R=–1) conditions at a frequency of 20 kHz, at ambient temperature, and controlled ambient air humidity, utilizing a Shimadzu USF-2000A ultrasonic fatigue testing system. The dimension of the final hourglass specimen used for ultrasonic fatigue tests is illustrated in Fig. 3(a) which was first designed using the internal software provided by the manufacturer of the ultrasonic fatigue test system, Shimadzu Scientific [36] by entering the values of Young's modulus and density obtained for LB-PBF AlSi10Mg to accomplish the required frequency range (19.5–20.5 kHz) in which the USF-2000A machine can start the test and to ensure that the highest level of stress is concentrated only on the gage section. Then, the natural frequency of the designed sample was confirmed by utilizing FEM analysis and it can be seen in Fig. 3(a) that the FEM calculated natural frequency was 20.24 kHz which was among the required range. Finally, It should be mentioned that the actual frequency of the whole ultrasonic fatigue testing system during testing was 20.02 kHz.

Additionally, the greatest displacement is seen at both the unsecured (free) end and the fixed end of the specimen. Throughout the testing procedure, careful monitoring of the specimen's temperature was conducted using an infrared thermometer (ETEKCITY Lasergrip 1022D). The aim was to restrict the temperature increase of the specimen to a maximum of 30 °C, thereby minimizing any potential impact on the outcomes. Moreover, a targeted flow of compressed air was directed specifically to the gauge section of the specimen, while intermittent alternations between driving pulses and pauses were implemented to alleviate thermal expansion effects induced by adiabatic heating. The duration of the pulses and pauses were established at 300 ms and 200 ms, respectively. Before testing, calibration of the piezoelectric transducer was performed using the Shimadzu Calibration Device (CDE-25), utilizing Young's modulus and density values obtained for LB-PBF AlSi10Mg. Additionally, the runout for the ultrasonic fatigue testing was configured to 10^9 cycles.

Additionally, quasi-static tensile tests were performed using the Instron 8822 servo-hydraulic test machine, which possesses a load capacity of 100 kN. All tensile specimens adhered to the specifications outlined in ASTM Standard E8M [37], with their dimensions depicted in Fig. 3(b). Axial deformation of the specimen's gauge section was monitored using an Epsilon mechanical extensometer featuring a gauge length of 20 mm. To ensure result consistency, at least two tension tests were performed for each set of specimens printed with varying geometries, employing a strain rate of 0.001 s^{-1}.

3. Experimental results

3.1. Microstructural and porosity analyses

The melt pool depth, d_p, and the overlap depth between the successive melt pools, d_o, were determined for parts manufactured in different geometries since the thermal history is anticipated to impact the melt pool morphology. These melt pool measures, which are shown in Table 3 in addition to the ratio of melt pool depth and melt pool overlap depth to layer thickness, t_L, were calculated using theMSFC-SPEC-3717 Technical Standard [38]. Fig. 4(a–e) shows the melt pools that were found in the

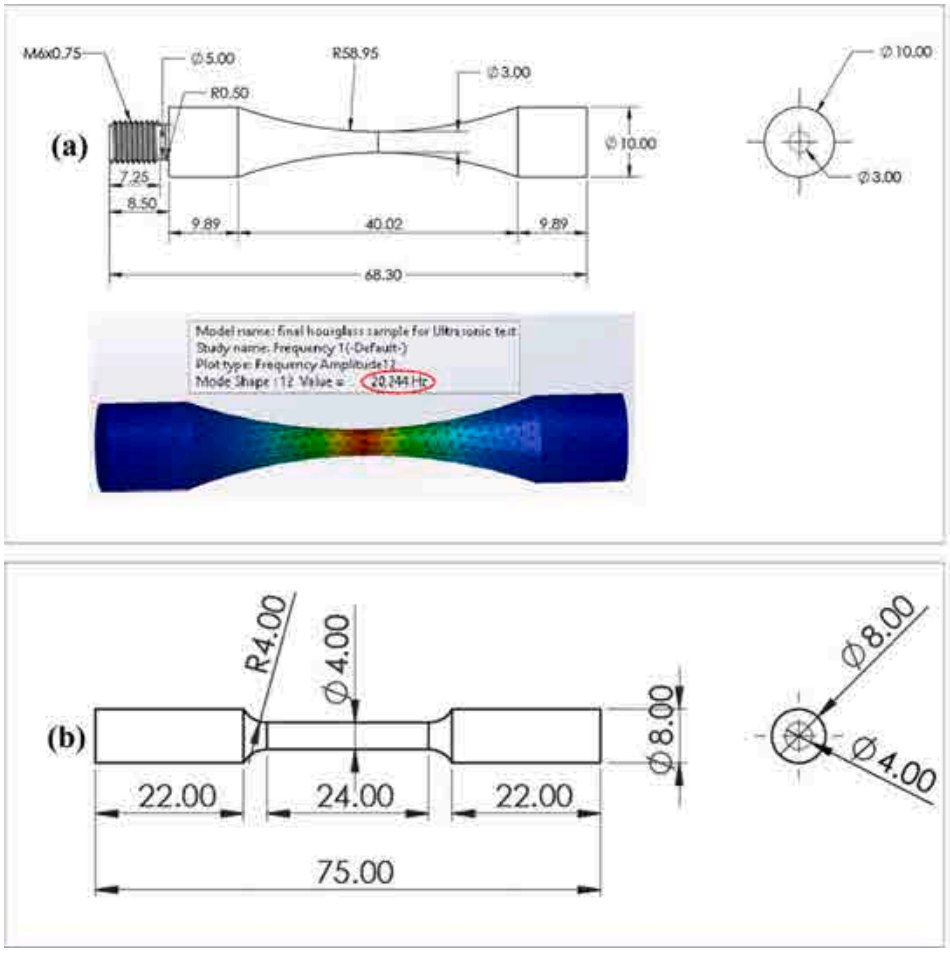

Fig. 3. (a) Dimensions of LB-PBF AlSi10Mg final hourglass sample of ultrasonic fatigue test, in addition to the FEM analysis used to confirm the natural frequency of the sample (b) dimensions of the quasi-static tensile test sample. All dimensions are in mm.

Table 3
Melt pool sizes obtained for parts manufactured with various geometries, including average melt pool depth, (d_p), average melt pool overlap depth, (d_o), and their ratio to layer thickness, (t_L).

Specimen	d_p (μm)(Mean ± SD)	d_p/t_L	d_o (μm) (Mean ± SD)	d_o/t_L
HG	69.7±16.7	2.3	46.6±12.1	1.55
SR	72.3±10.2	2.4	45.1±7	1.50
SB	73.5±12.9	2.5	45.4±10.9	1.51
LB	76.9±13.1	2.6	53.5±9.9	1.78
LR	80.6±20.1	2.7	58.2±17.1	1.94

middle of the top layer (i.e. very last layer) of the half-built HG, SR, SB, LB, and LR, respectively. The observed waviness in the specimens is because of the surface roughness of the as-printed top surface (i.e., transverse cross-section) of half-bult specimens. For each of the micrographs shown in Fig. 4, the parameters of the melt pools, including melt pool depth (yellow arrows) and overlap depth (red arrows) were determined using ImageJ software. LR and LB specimens were found to have a larger average melt pool depth of ~80.6 μm and ~76.9 μm, respectively. On the other hand, smaller average melt pool depths of ~73.5 μm and ~72.3 μm were obtained for SB and SR, respectively, while the HG sample showed the smallest average melt pool depth with ~69.7 μm. Alongside the average values of melt pool depth, it was observed that the average value of melt pool overlap depth, d_o, also varied depending on the part geometry. The melt pool overlap depth increased from ~45.1 μm in the SR to ~58.2 μm in the LR.

Fig. 5(a–e) illustrates the SEM micrographs in longitudinal cross-sections of LB-PBF AlSi10Mg specimens with different geometries after stress relief heat treatment. Very similar microstructural changes are observed for specimens with various geometries and stress relieving at

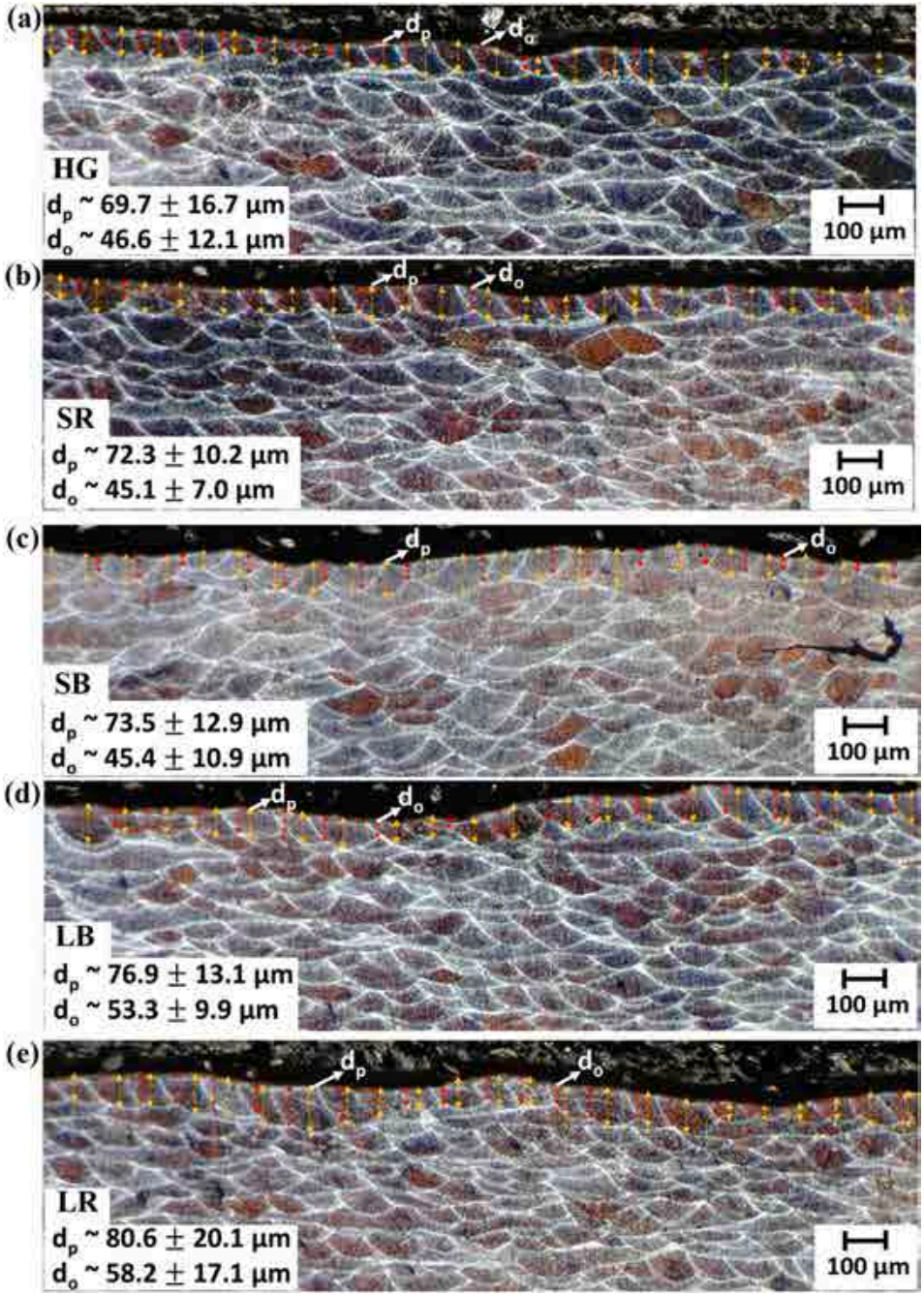

Fig. 4. Melt pool micrographs accompanied by the mean measurements of melt pool depth, d_p, and overlap depth, d_o, for (a) HG (b) SR (c) SB (d) LB (e) LR.

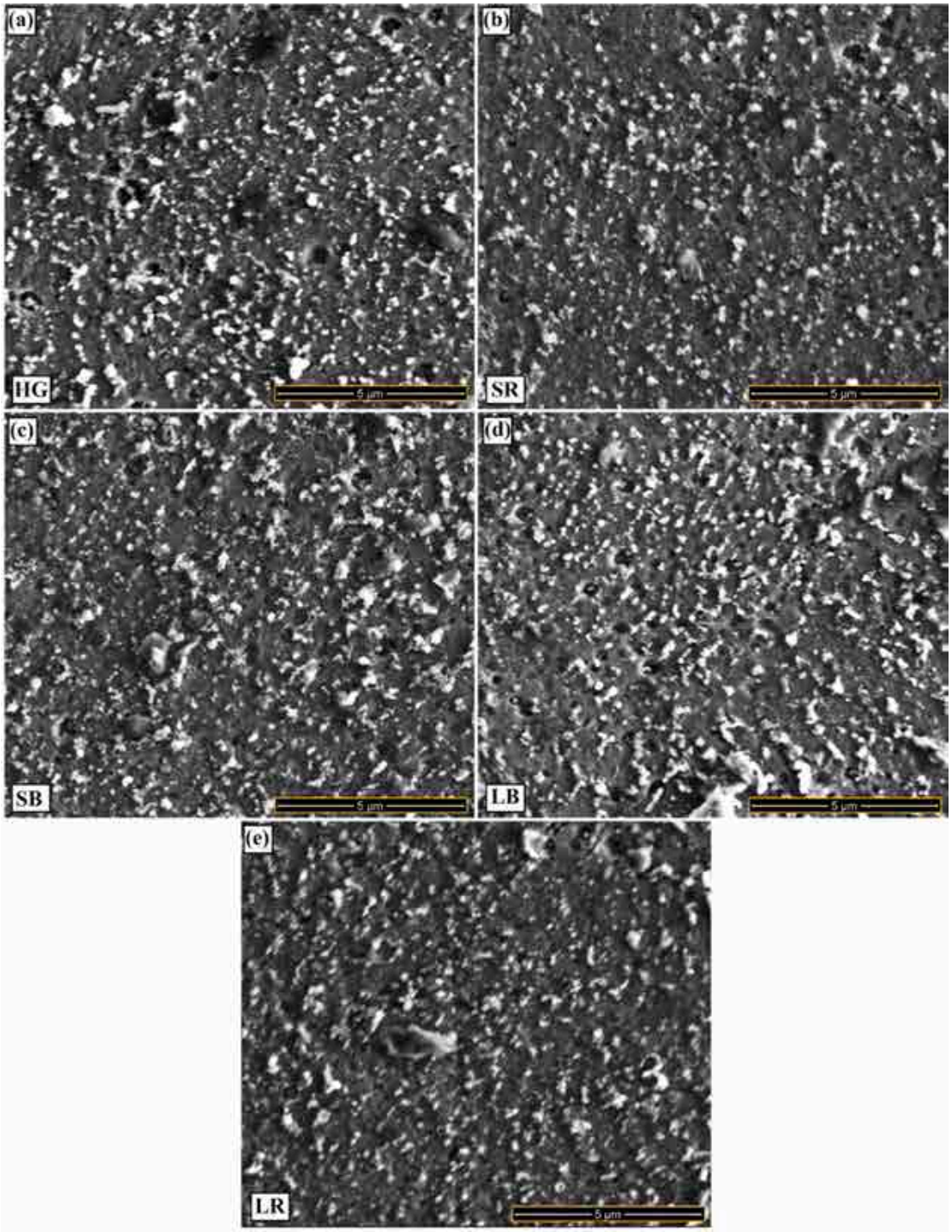

Fig. 5. SEM images in longitudinal cross-sections of LB-PBF AlSi10Mg specimens after stress relief (300 °C for 2 h) for (a) HG, (b) SR, (c) SB, (d) LB, (e) LR.

300 °C for 2 h causes an almost complete disintegration of the initial silicon network and cells into individual Si particles, followed by particle coarsening for all the geometries as it was also observed in the literature for the same stress relieve condition in LB-PBF AlSi10Mg material [39–41]. Therefore, the SEM micrographs showed that the variation in part geometry and size did not affect the structure of the Si-cells, and all the initial Si-cell boundaries could not be seen anymore after stress relieving in any part.

The alteration in the thermal history shown by the melt pool morphology is anticipated to impact the spreading and population of gas porosities. To acquire a more comprehensive knowledge of defect distribution in parts printed with various geometries, a 3D porosity analysis was performed using X-ray CT at the gauge section of hourglass ultrasonic fatigue specimens. Fig. 6(a–e) displays the histograms of defects along with the total volume percentage of defects derived from the 3D defect analysis coupled with the reconstructed X-ray CT images of the gage section for HG, SR, SB, LB, and LR specimens. It is also noteworthy to state that the outcomes derived from the three-dimensional porosity assessment were standardized through the process of dividing the count of imperfections by the respective scanned volumes. It is seen in Fig. 6 that between the five groups of specimens, LR and LB specimens had the lowest total volume percent of defect of 0.062 % and 0.067 %, respectively, while SR and SB samples had the highest volume percent of defect of 0.087 % and 0.084 %, respectively. HG Sample also showed an

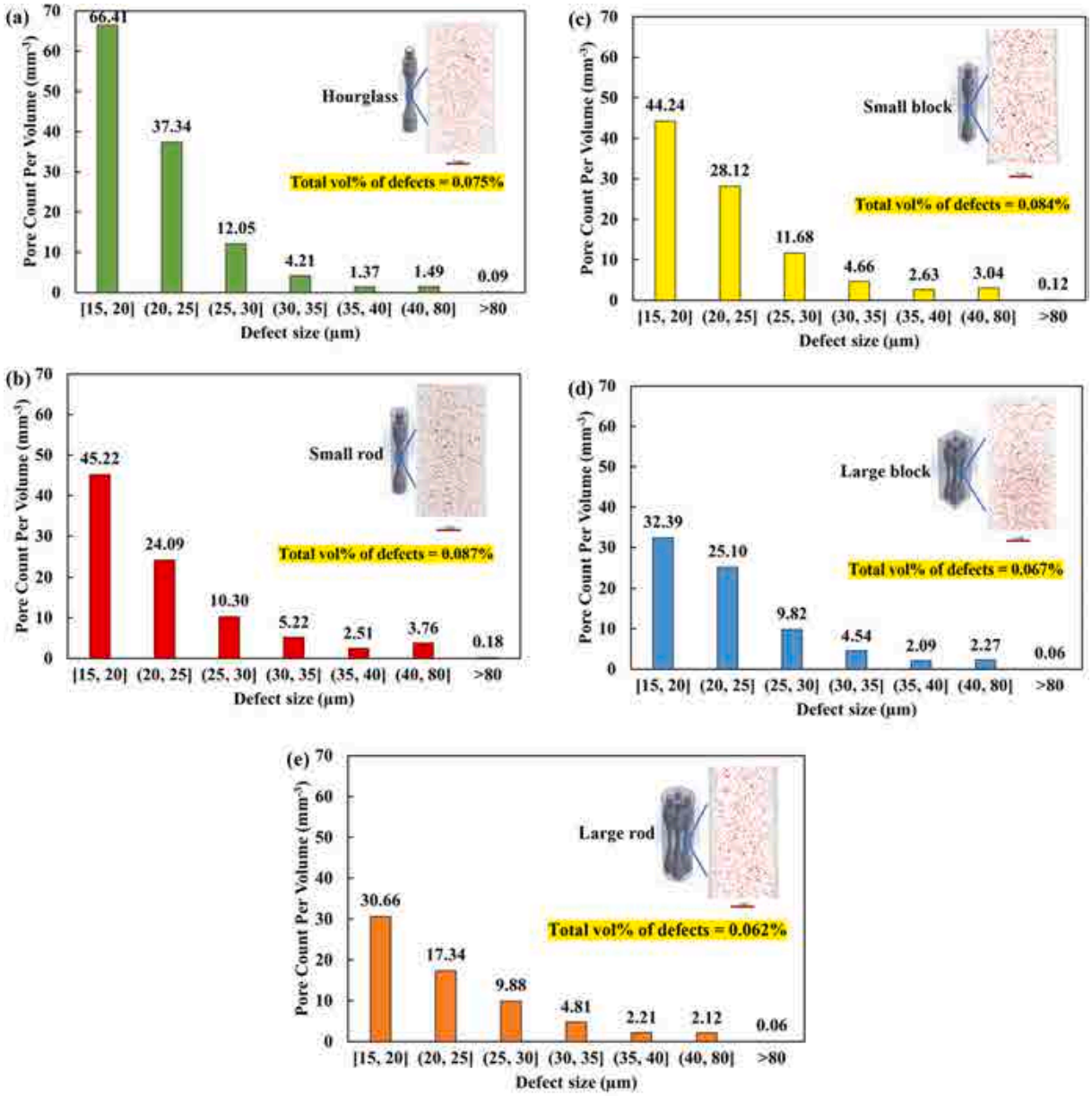

Fig. 6. Histograms illustrating the defects' size acquired using 3D image analysis alongside X-ray CT images showing defects' distribution in the (a) HG (b) SR (c) SB (d) LB (e) LR.

intermediate total volume percentage of defect of 0.075 %. Looking only at the number of defects greater than 80 µm in diameter, which are usually the defects responsible for fatigue crack initiation [42], LR, LB, and HG specimens had the fewest at 0.06, 0.06, and 0.09 pore count per volume, respectively, while SR and SB specimens showed the most at 0.18 and 0.12, respectively. Furthermore, it was observed that the greatest defect size was smaller for LR (97 µm) and LB (100 µm) compared to the SB (121 µm), SR (107 µm), and HG (108 µm) specimens. While fatigue failure predominantly occurs at localized points, the existence of supplementary volumetric defects, especially if they are substantial and located near the surface (i.e., subsurface), could elevate the likelihood of crack initiation at a lower cycle count, thereby leading to a diminished fatigue response. However, surface defects, such as those released by machining and polishing, cannot be characterized that easily by XCT.

It should also be mentioned that clear discrepancies can be observed in the number of imperfections smaller than 20 µm in diameter, which is the typical size of entrapped gas porosities, which were realized for specimens manufactured from different part geometries. HG specimens with the lowest cross-sectional area had the highest number of pores per mm^3 (66.41), followed by the SR specimen (45.22), SB specimen (44.24), LB specimen (32.39), and LR specimen, which had the lowest number of pores smaller than 20 µm in diameter at 30.66 per mm^3.

3.2. Tensile flow curves

The engineering flow curves derived from uniaxial tensile tests for HG, SR, SB, LB, and LR specimens are illustrated in Fig. 7. Additionally, Table 4 lists the average, as well as the higher and lower values, of the tensile characteristics which include yield stress (σ_y), ultimate tensile strength (σ_u), and strain of fracture (ε_f) derived from two consecutive trials for each category of sample. As was observed from the XCT porosity analysis in Fig. 6, the five different print geometries each had a different degree of volumetric defect. However, these differences did not exert a considerable influence on the tensile characteristics of the LB-PBF AlSi10Mg specimens, and the same behavior was seen on the

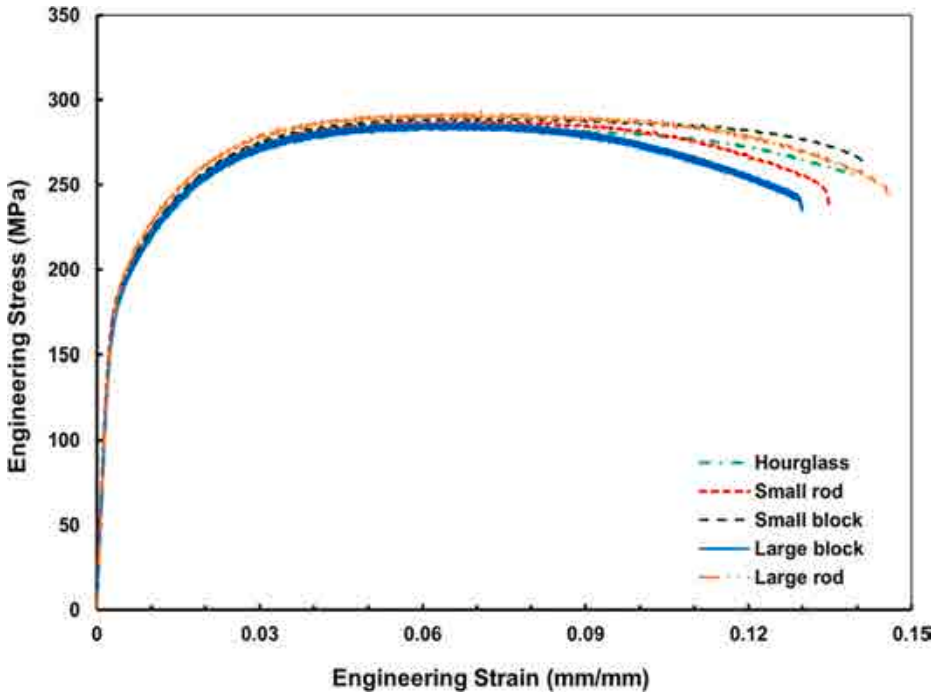

Fig. 7. Engineering flow curves resulting from tensile tests of LB-PBF AlSi10Mg specimens machined from components with diverse geometries.

Table 4
Uniaxial tensile characteristics of LB-PBF AlSi10Mg specimens that were machined from parts with varying geometries.

Properties	HG	SR	SB	LB	LR
E (GPa)	67.9±0.4	67.4±0.8	67.3±0.6	70.1±0.9	69.8±0.9
σ_y (MPa)	182.5±2.5	191±5	184.5±6.5	183.5 ±3.5	193±4
σ_{UTS} (MPa)	281±4	280.5±7.5	285.5±4.5	283.3 ±3.7	287.5±6.5
ε_f (mm/mm)	0.146 ±0.003	0.131 ±0.003	0.138 ±0.004	0.129 ±0.01	0.142 ±0.006

effect of part geometry on the tensile properties of LB-PBF 17–4 PH SS [30]. The tensile properties did not significantly alter since the changes in the morphology of the silicon network, as was shown in Fig. 5 with the SEM micrographs, were very similar for the specimens with different geometries.

3.3. Fatigue and fractography analysis

Defects like pores and LoFs may negatively impact the structural durability of LB-PBF parts when exposed to cyclic loading. This is because these defects influence the localized stress field and create stress concentration. Therefore, it is anticipated that any deviations in the size, position, and shape of defects (as shown in Fig. 6) would result in fluctuations in the fatigue strength of LB-PBF AlSi10Mg in the VHCF domain. A comparison of stress-life data for each part geometry is presented in Fig. 8 graphically, and all the ultrasonic fatigue test results are listed in Table A1 in the Appendix A section. To better compare the fatigue life of the LB-PBF AlSi10Mg specimens with different geometry, the Basquin equation [43] is used which correlates the fatigue stress amplitude (σ_a) to the cycles to failure (N_f) by using fatigue strength coefficient (σ'_f) and fatigue strength exponent (b). The following equation is fitted to each set of experimental data as shown in Fig. 8:

$$\sigma_a = \sigma'_f (2N_f)^b \quad (1)$$

Based on the Basquin equation, for a given σ'_f, smaller values of b correspond to a shallower slope and therefore higher fatigue limit. The Basquin equation was used to fit a line on the fatigue data in the current study and the results are summarized in Table 5. By choosing a fixed number of cycles to failure in the VHCF regime (*e.g.*, $N_f = 10^8$), the fatigue strength at that cycle (σ'_8 for $N_f = 10^8$) was extracted to compare VHCF behavior in different specimens. According to the calculated data (shown in Table 5), the LR and LB specimens had the highest fatigue strength at 10^8 cycles, while the HG, SR, and SB specimens showed a much lower value of σ'_8. Fig. 8 demonstrates that the geometry of the part significantly affects the fatigue life of LB-PBF AlSi10Mg specimens in the very high cycle regime, specifically at lower stress amplitudes of 91 and 102 MPa. LR and LB specimens have the longest fatigue lifespans, followed by HG, SB, and SR specimens, respectively. The alterations in defect population and size exhibited in Fig. 6 may partially explain the fatigue life data shown in Fig. 8. The LR and LB specimens with the highest fatigue strength had a lower porosity in the range of greater than 80 μm. On the other hand, the SR and SB specimens with the highest porosity had the shortest fatigue life. HG samples generally showed a better fatigue performance compared to SR and SB since they had less porosity, especially in the range of greater than 80 μm. In the VHCF domain, where the deformation is globally elastic and defects cause larger stress concentrations compared to LCF or HCF regimes, it is widely recognized that larger defects have a supplementary substantial effect on the fatigue performance of the material [42].

Fractography was conducted on the failed specimens to better comprehend the factors that were responsible for the crack initiation and final failure in the LB-PBF AlSi10Mg specimens. Representative fracture surfaces of HG, SR, SB, LB, and LR specimens, all of which were subjected to the stress amplitude of 91 MPa and 102 MPa, are shown in Fig. 9(a–e) and Fig. 10(a–e), respectively.

Since defects have various shapes and are at different distances from the surface, we need to establish the pertinent criterion for evaluating the impact of imperfections. In this regard, the equivalent dimension of a critical defect that causes crack initiation can be expressed with $\sqrt{a_c}$ (i.e., square root area of critical defect) in terms of a fracture mechanics concept [44,45]. Hence, the equivalent defect size was measured according to the Murakami method [46] to consider the impact of the defect's morphology and distance from the surface. Table 6 displays the

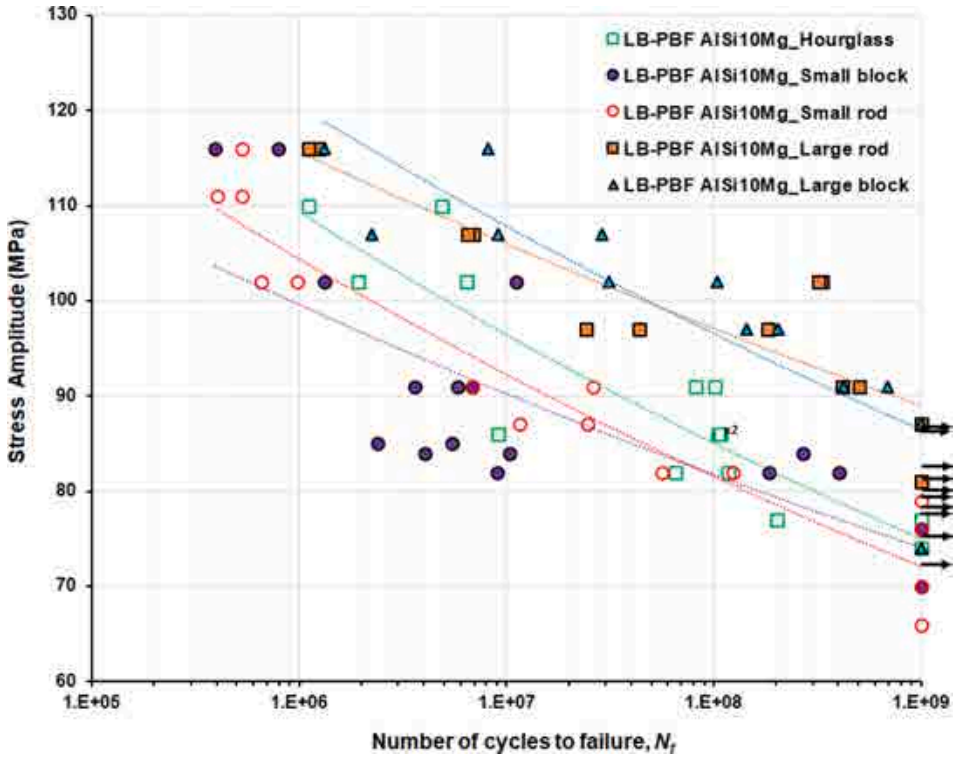

Fig. 8. Stress-life (S-N_f) data for LB-PBF AlSi10Mg printed in five different initial geometries and tested using the ultrasonic fatigue test method under fully reversed loading at 20 kHz.

Table 5
The calculated fatigue strength coefficient (σ'_f), fatigue strength exponent (b), and fatigue strength at 10^9 cycles (σ'_9) of LB-PBF AlSi10Mg specimens with different geometry.

Specimen	σ'_f (MPa)	b	σ'_9 (MPa)
HG	232.3	−0.055	84.3
SR	218.93	−0.054	80.9
SB	180.03	−0.043	81.5
LB	233.73	−0.048	96.5
LR	195.34	−0.038	97.0

size, type (i.e., surface, subsurface, or internal defect), and distance from the surface of critical defects that originate failures in 30 different specimens. The equivalent critical defect area was measured using ImageJ software which is highlighted with orange color in Fig. 9 and Fig. 10 for the images of higher magnification.

In the cases of stress amplitude of 91 MPa, Fig. 9 shows that cracks are initiated from defects located at or near the surface except for an LR sample in which the crack originated from an interior defect. Table 6 shows that the critical defect size plays a key role in the fatigue life of the specimen at a lower stress amplitude of 91 MPa. The longest fatigue life was observed for the LR specimen (N_f = 5.21E+08) with the smallest equivalent critical defect size of ~41.63 μm, followed by the LB specimen (N_f = 4.24E+08) with an equivalent critical defect size of ~47.03 μm, and the shortest fatigue life was observed for the SB specimen (N_f = 5.78E+06) with the highest equivalent critical defect size of about 111.27 μm.

Fig. 10 shows that in the cases of specimens failing at a higher stress amplitude of 102 MPa, the location of critical defects is more dispersed within the cross-section. The location of critical defects also plays a pivotal role in determining fatigue life, as surface defects tend to be more critical than internal defects [47]. As shown in Table 6, at this stress level, LR and LB samples once again showed the highest fatigue life with N_f = 3.20E+08 and N_f = 1.04E+08, respectively, with also having a smaller critical defect size of ~65.5 μm and ~83.91 μm compared to HG (N_f = 1.94E+06), SB (N_f = 1.33E+06) and SR (N_f = 6.60E+05) samples with the larger critical defect size of ~91.25 μm, ~106.5 μm and ~172.19 μm, respectively. A significant variation in fatigue life was observed between LB (N_f = 1.04E+08) and HG (N_f = 1.94E+06) samples, but the difference between critical defect size was not large enough to explain such a substantial variation in the number of cycles to failure. This variation can be attributed to the location of critical defects as surface defects are more damaging than interior defects, especially under lower stress amplitude in the VHCF regime [5,48–50]. The fisheye pattern was observed for both LR and LB specimens, with the failures originating from internal critical defects with a distance to the surface of ~490.2 μm and ~583.2 μm, respectively, which were much deeper than those observed for defects in HG, SR, and SB samples.

It was found from fractography analysis that both factors of size and location of the critical defect had a remarkable effect on the fatigue response of LB-PBF AlSi10Mg specimens. However, Fig. 11 has been provided to show what would be the most important influence factor on the VHCF response of specimens with different geometry. Therefore, one sample from hourglass geometry (i.e., the specimen with the lowest cross-sectional area) and another sample from large rod geometry (i.e., the specimen with the highest cross-sectional area) have been selected. The LR sample despite having a much larger critical defect size (~139.86 μm) had a higher number of cycles to failure at a stress amplitude of 97 MPa, while the HG sample with a much smaller critical defect size (~67.32 μm) showed a lower number of cycles to failure even at smaller stress amplitude of 91 MPa. This may indicate that the location of the critical defect can be the most important influence factor on the VHCF response of LB-PBF AlSi10Mg specimens as the crack origin observed for the LR sample was due to an internal defect forming a fisheye pattern compared to the cracks originated from the surface for HG sample.

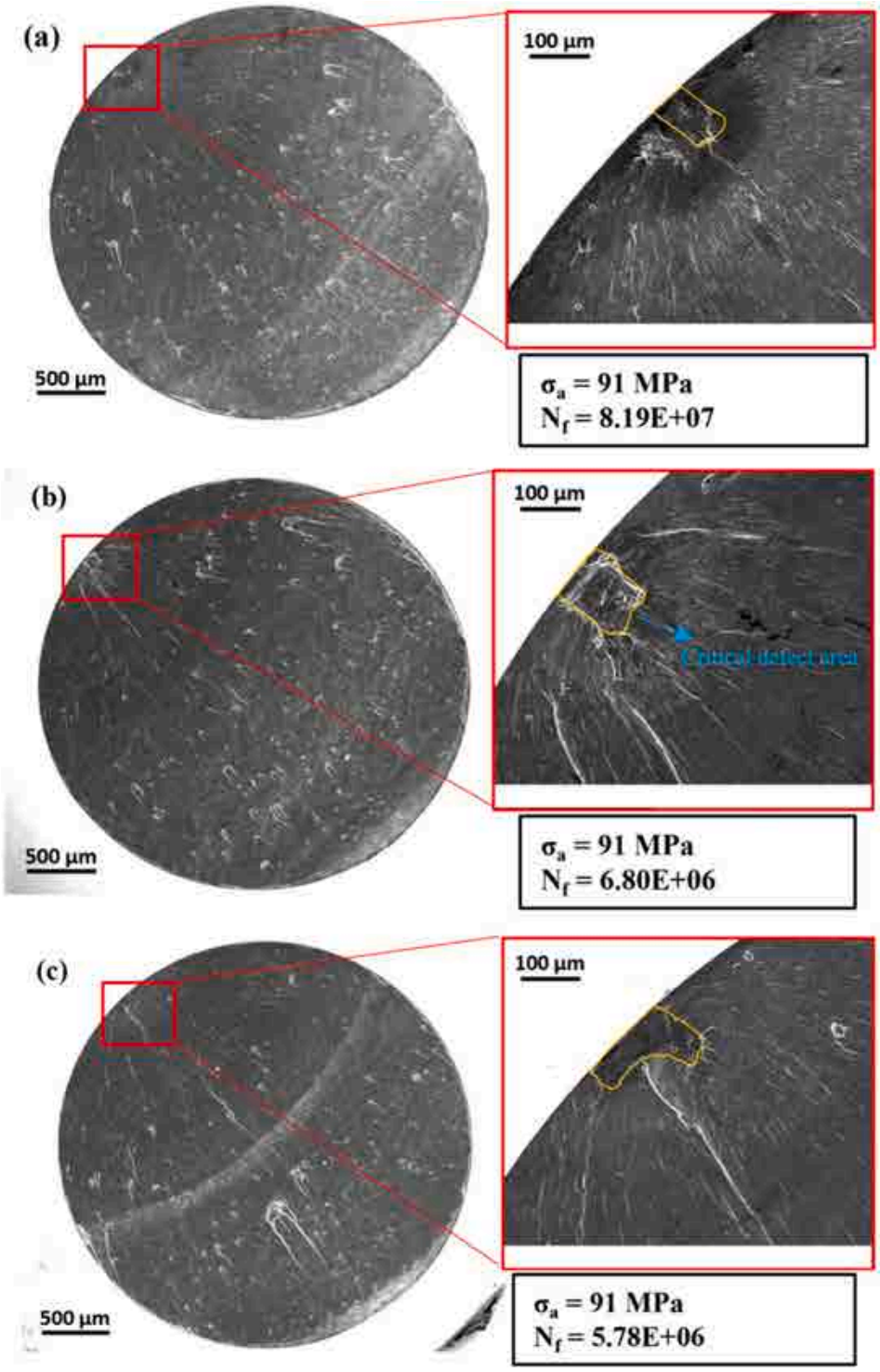

Fig. 9. Descriptive fracture surfaces of LB-PBF AlSi10Mg for specimens from (a) HG (b) SR (c) SB (d) LB (e) LR. All specimens were exposed to 91 MPa stress amplitude at a frequency of 20 kHz.

4. Discussion

4.1. Probabilistic S-N curves

The S–N_f data in Fig. 8 show a large scatter in the experimental data. Accordingly, Probabilistic S-N curves (P-S-N curves) were incorporated to investigate the geometry effect in a statistical framework. The logarithm of the number of cycles to failure was assumed to be normally distributed, with the mean linearly decreasing with the logarithm of the applied stress amplitude and constant standard deviation. The standard deviation, the slope, and the intercept of the mean were estimated by applying the maximum likelihood principle, to consider both failure and runout data. Fig. 12 presents the estimated P-S-N curves. In Fig. 12(a–e) the median, the 10-th, and the 90-th percentile P-S-N curves are plotted for each different geometry, and Fig. 12(f) assesses the median P-S-N curves for all investigated geometries.

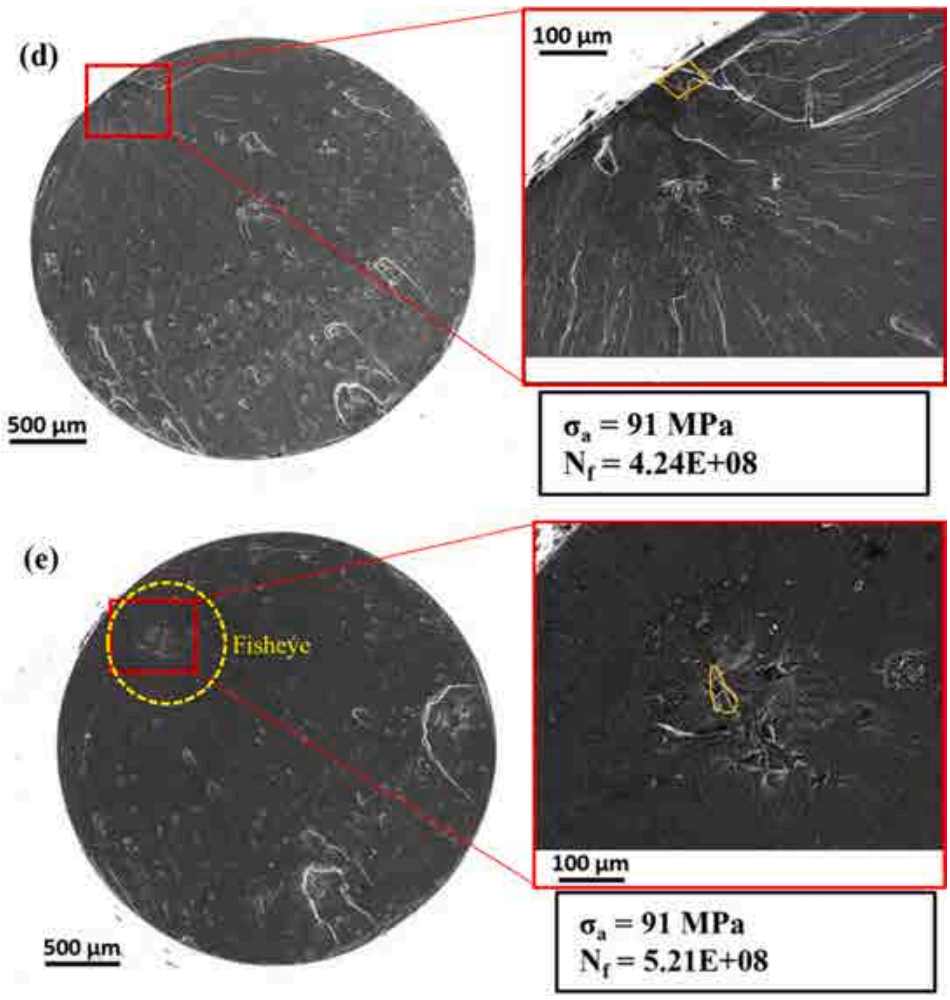

Fig. 9. (*continued*).

Fig. 12(a–e) shows that the estimated P-S-N curves agree with the experimental data, with about 80 % of the data within the 10-th and the 90-th P-S-N curves for all investigated datasets. The linear trend is appropriate for all datasets since an asymptotic trend (i.e., endurance limit) is not visible close to 10^9 cycles. A fatigue limit at 10^9 cycles in the VHCF life range can be excluded. The median curves in Fig. 12(f) show that the geometry of AM parts significantly affects the fatigue response in the investigated VHCF range. In particular, the median P-S-N curves for LB and LR are very close, with the same slopes. On the other hand, the curves for HG, SB, and SR specimens follow different slopes, with fatigue strengths at 10^9 cycles that are significantly below the fatigue strengths of LB and LR. In particular, the slopes of HG and SB are similar, whereas it is smaller for SR.

For a better comparison of the VHCF responses, all the experimental failures were moved at a reference number of cycles, N_{ref}, corresponding to 10^9 cycles, according to the procedure shown in Fig. 13. Each failure (circle marker in Fig. 13) identifies a specific α-th quantile P-S-N curve that can be followed up to 10^9 cycles to define the failure shift at N_{ref} (star marker in Fig. 13). This procedure was repeated for each experimental failure and permitted to statistically investigate the influence of the geometry effect.

Fig. 14 compares the fatigue strength shifted at 10^9 cycles for the investigated geometries. The experimental data and the 95 % confidence interval for the mean are plotted in Fig. 14. According to Fig. 14, the experimental failures shifted at N_{ref} can be divided into two groups: LB and LR, belonging to the first group (Group (1), are characterized by a similar median fatigue strength, close to 90 MPa, which is significantly higher than that of the datasets belonging to the second group (Group (2), which includes HG, SB, and SR (close to 70 MPa).

The fatigue strengths and the confidence intervals for the mean of the two groups do not overlap, confirming that the difference can be considered statistically significant and that the geometry effect exerts a notable impact on the fatigue response. When specimens were obtained from larger parts the fatigue response was enhanced, regardless of the shape (rod or block). One possible reason is that defects close to the free surface are more detrimental and that their effect can be mitigated as the distance from the free surface of the part increases. Another interesting aspect is the VHCF strength scatter, which varied depending on the dataset and was different between the two groups. Indeed, the experimental scatter tended to be smaller for LB and LR, being very close for these two datasets. The ratio between the 95 % confidence interval amplitude, $CI_{95\%}$, and the median fatigue strength value s_{50}, ($\frac{CI_{95\%}}{s_{50}}$ ratio) is equal to 5 % and 7 % for the LB and the LR specimens, respectively, with an average $\frac{CI_{95\%}}{s_{50}}$ ratio equal to 6 % for this group. On the other hand, the experimental variability was significantly larger for the second group. The average value of the $\frac{CI_{95\%}}{s_{50}}$ ratio for this group is equal to 9 %. In this second group, however, the experimental variability was not constant, being smaller for SR ($\frac{CI_{95\%}}{s_{50}}$ ratio equal to 5 %) and very large for SB ($\frac{CI_{95\%}}{s_{50}}$ ratio equal to 14 %), even if the average value of the VHCF strength is similar. The different experimental variability between Group (1) and Group (2) was also verified with a Lavene test, which provided a p-value close to 0.3 % and therefore confirmed that the experimental scatter of these two groups was statistically different. On

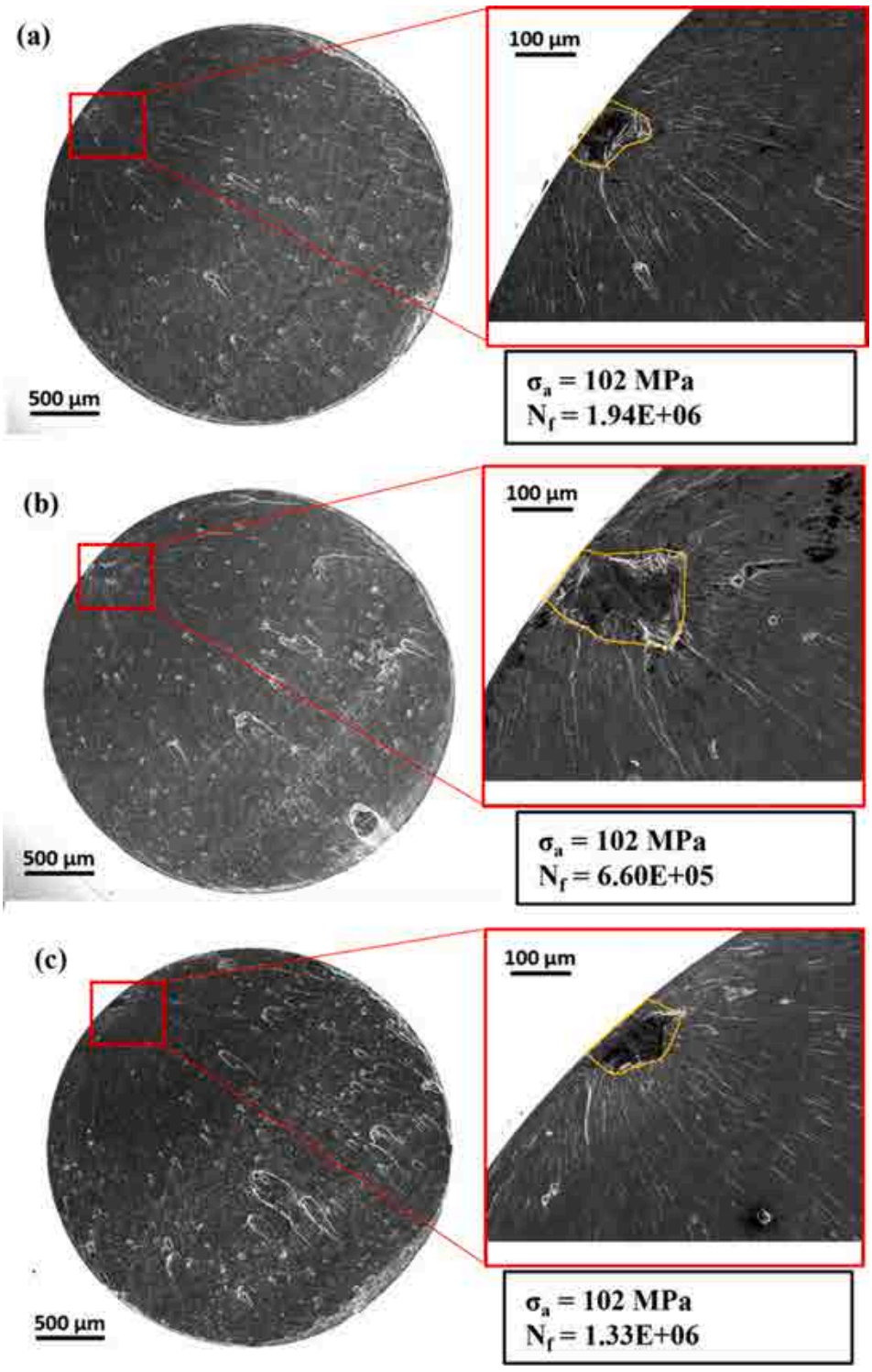

Fig. 10. Descriptive fracture surfaces of LB-PBF AlSi10Mg for specimens from (a) HG (b) SR (c) SB (d) LB (e) LR. All specimens were subjected to 102 MPa stress amplitude at a frequency of 20 kHz.

the other hand, the p-value computed with a Lavene test between the datasets belonging to Group (1) (LB and LR) was close to 70 %, confirming that there was not a significant difference between LB and LR variance at the investigated reference number of cycles. By considering the specimens belonging to Group (2), the p-value associated with the Lavene test was close to 6 %, slightly above a common 5 % significance level.

This analysis proved that the geometry effect was relevant and affected the fatigue strength in the VHCF life region. In particular, the distance from the free printing surface affected the fatigue response, with specimens obtained from larger parts, regardless of the shape (rod or block), characterized by larger VHCF response and smaller variability than that obtained from small parts (SB and small box) and HG parts.

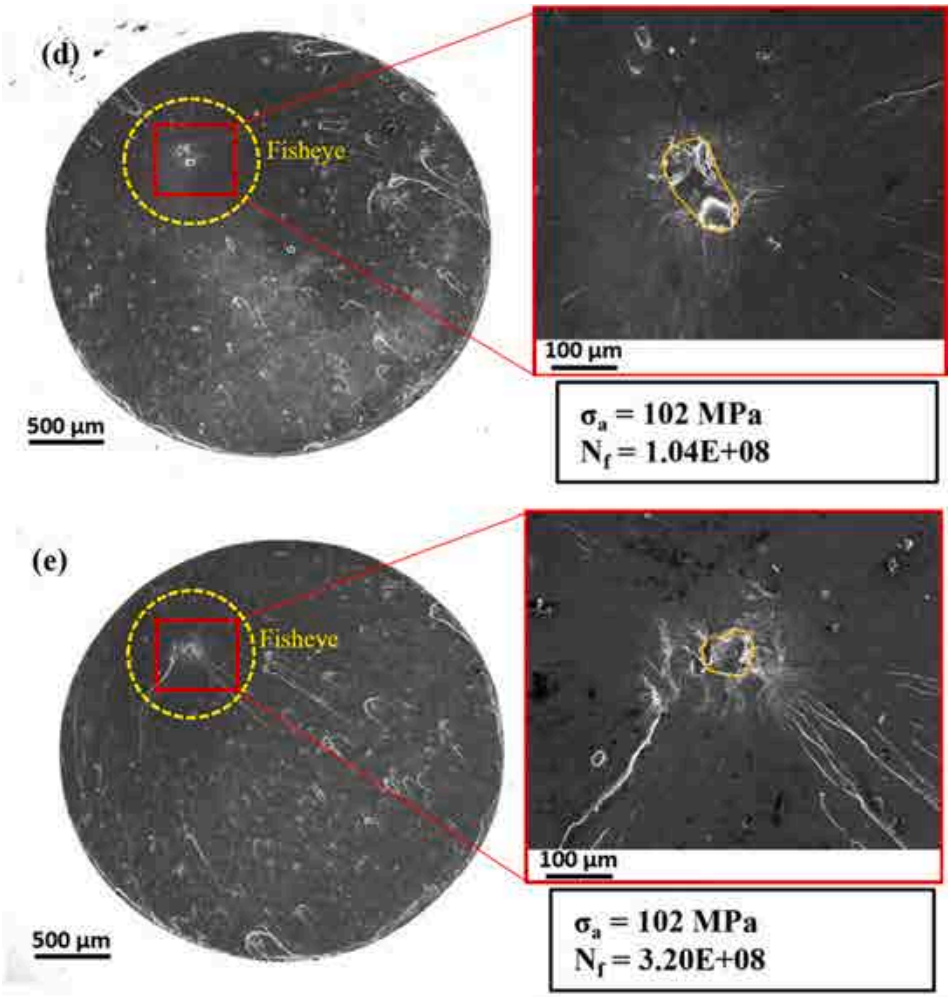

Fig. 10. (*continued*).

4.2. Statistical analysis of defect size

The analysis of the defects at the source of fatigue failure, i.e., the critical defects, is of vital importance in a structural integrity context. In particular, according to [46], the defect size can strongly influence the fatigue crack initiation. In the subsequent analysis, the characteristic size of defects was presumed to be the square root of the area of the defect projected onto a plane perpendicular to the direction of the maximum applied stress. To compare defects with irregular morphologies and different locations within the cross-section, the rules provided in [44] and based on fracture mechanics concepts were followed to assess an equivalent defect size (Table 6). The equivalent defect size was considered as a random variable, $\sqrt{A_c}$, following the Largest Extreme Value Distribution (LEVD) and with cumulative distribution function, $F_{\sqrt{A_c}}(\sqrt{a_c})$, reported in Eq. (2):

$$F_{\sqrt{A_c}}(\sqrt{a_c}) = e^{-e^{-\left(\frac{\sqrt{a_c}-\mu_{\sqrt{A_c}}}{\sigma_{\sqrt{A_c}}}\right)}} \quad (2)$$

being $\mu_{\sqrt{A_c}}$ and $\sigma_{\sqrt{A_c}}$ the location and the scale parameters, respectively. According to [51], the lower case denotes the random variable, whereas the upper case its realization. The parameter estimation was conducted by applying the Least Square Method. Fig. 15 plots the experimental data in a Gumbel plot, together with the estimated LEVD functions by using the value of $\sqrt{a_c}$ provided in Table 6 for the investigated geometries and configurations.

According to Fig. 15, the trend of the LEVDs agrees with the trend of the experimental data on the S-N plot. Indeed, fatigue failures in LB and LR originated from defects having sizes smaller than those of HG, SB, and SR. The difference was, however, not so large, with the data characterized by a large scatter, as expected for irregular defects typical of AM parts. Moreover, the dataset numerosity was not so large, thus possibly affecting the results of the analysis. However, the trend in Fig. 15 is clear, confirming that defects tended to be smaller in LB and LR, thus enhancing their fatigue response in the investigated HCF-VHCF life regimes.

4.3. The effect of part geometry on thermal history

The observed disparities in the melt pool size of samples with various geometries, displayed in Fig. 4, indicate that the change in the specimen geometry plays a key role in the thermal history encountered by the part over the LB-PBF process. There is a possibility that the local energy density will change when the heat dissipation conditions are different for samples with varied geometries. This helps to explain the varied defect levels that are seen in samples with various geometries. The decreased temperature of the solidified material, which provides a base for the formation of a new layer, maybe the cause of the shorter melt pool depths seen in the HG, SR, and SB specimens. In samples with smaller cross-sectional areas, there is typically less material volume overall. This can result in faster heat dissipation from the part during the printing process, as there is less material to retain and conduct heat [52]. Therefore, the temperature at which a fresh layer is created onto the

Table 6
Fractography results of some LB-PBF AlSi10Mg specimens failed under ultrasonic fatigue loading at 20 kHz.

Specimen ID	Stress amplitude (MPa)	Number of cycles to failure, N_f	Defect type	Equivalent critical defect size, $\sqrt{a_c}$ (μm)	Distance of defect from the surface (μm)
LR17	91	5.21E+08	Internal Defect	41.63	303.568
LB10	91	4.24E+08	Surface Defect	47.03	–
HG17	91	8.19E+07	Surface Defect	79.56	–
SR13	91	6.80E+06	Surface Defect	108.10	–
SB3	91	5.78E+06	Surface Defect	111.27	–
LR15	102	3.20E+08	Internal Defect	65.50	490.2
LB14	102	1.04E+08	Internal Fisheye Defect	83.91	583.2
HG8	102	1.94E+06	Surface Defect	91.25	–
SB18	102	1.33E+06	Subsurface Defect	106.50	19.687
SR5	102	6.60E+05	Subsurface Defect	172.19	27.111
LR5	97	4.40E+07	Surface Defect	67.18	–
LR6	97	1.83E+08	Internal Fisheye Defect	139.86	686.66
LR11	91	5.05E+08	Surface Defect	32.88	–
LR14	102	3.35E+08	Internal Fisheye Defect	86.05	838.1
LB5	107	2.90E+07	Internal Defect	79.03	116.4
LB7	97	1.44E+08	Two Adjacent Surface Defects	63.41	–
SB4	82	9.01E+06	Surface Defect	100.77	–
SB8	91	6.80E+06	Surface Defect	88.70	–
SB10	84	2.69E+08	Internal Defect	58.00	40.1
SB11	84	1.03E+07	Subsurface Defect	77.64	16.7
SB12	82	4.02E+08	Internal Defect	54.09	55.5
SB14	91	3.60E+06	Cluster of Surface Defects	124.84	–
SR8	82	1.23E+08	Subsurface Defect	84.42	19.4
SR10	102	9.80E+05	Subsurface Defect	89.82	19.7
SR15	87	2.46E+07	Surface Defect	85.04	–
SR17	91	2.60E+07	Two Adjacent Surface Defects	87.59	–
HG3	91	1.02E+08	Surface Defect	67.32	–
HG6	82	1.18E+08	Surface Defect	63.37	–
HG9	82	6.50E+07	Subsurface Defect	98.25	22.6
HG10	86	1.07E+08	Subsurface Defect	82.58	37.5
HG11	86	9.08E+06	Surface Defect	88.26	–

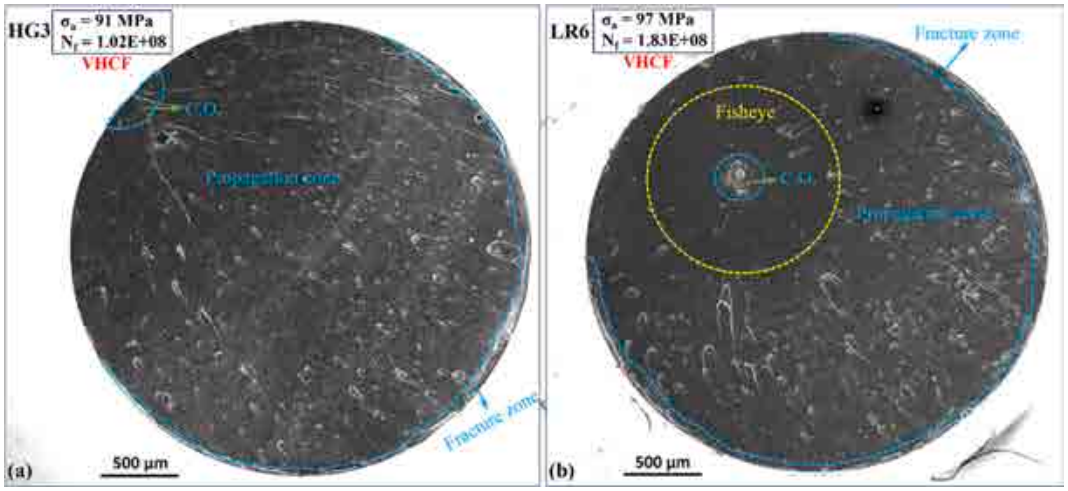

Fig. 11. Fracture surface morphology of the specimens failed in the VHCF regime: (a) Hourglass (HG3) (b) Large rod (LR6). C.O.: crack origin.

solidified material might be lower in samples with smaller cross-sectional areas [30,53]. This lower temperature leads to a faster cooling rate that is experienced by HG, SR, and SB specimens with less cross-sectional area in comparison to the LB and LR specimens with larger cross-sectional area. However, the greater size of the melt pool in LB and LR is an indicator of a decreased cooling rate that these specimens underwent throughout the manufacturing process because of their larger cross-sectional areas. The increased temperature of the solidified material, upon which a new layer is deposited, is most likely the cause of this slower cooling rate. Finally, the increased rate of cooling, and therefore the faster solidification in HG, SR, and SB specimens, reduces the duration that the gas pores have to leave the melting pool, which ultimately leads to the transformation of the gas pores into entrapped gas pores [54].

4.4. The effect of part geometry on volumetric defects and fatigue performance

According to a recent study, volumetric defects formed during LB-PBF that are detected using an X-ray CT scan can be accurately categorized as entrapped gas pores, keyholes (KHs), and LoFs by using multiple morphological features that have fairly minor overlaps between the three distinct defect types and their corresponding ranges [55]. They reported that the most distinctive characteristic between KHs

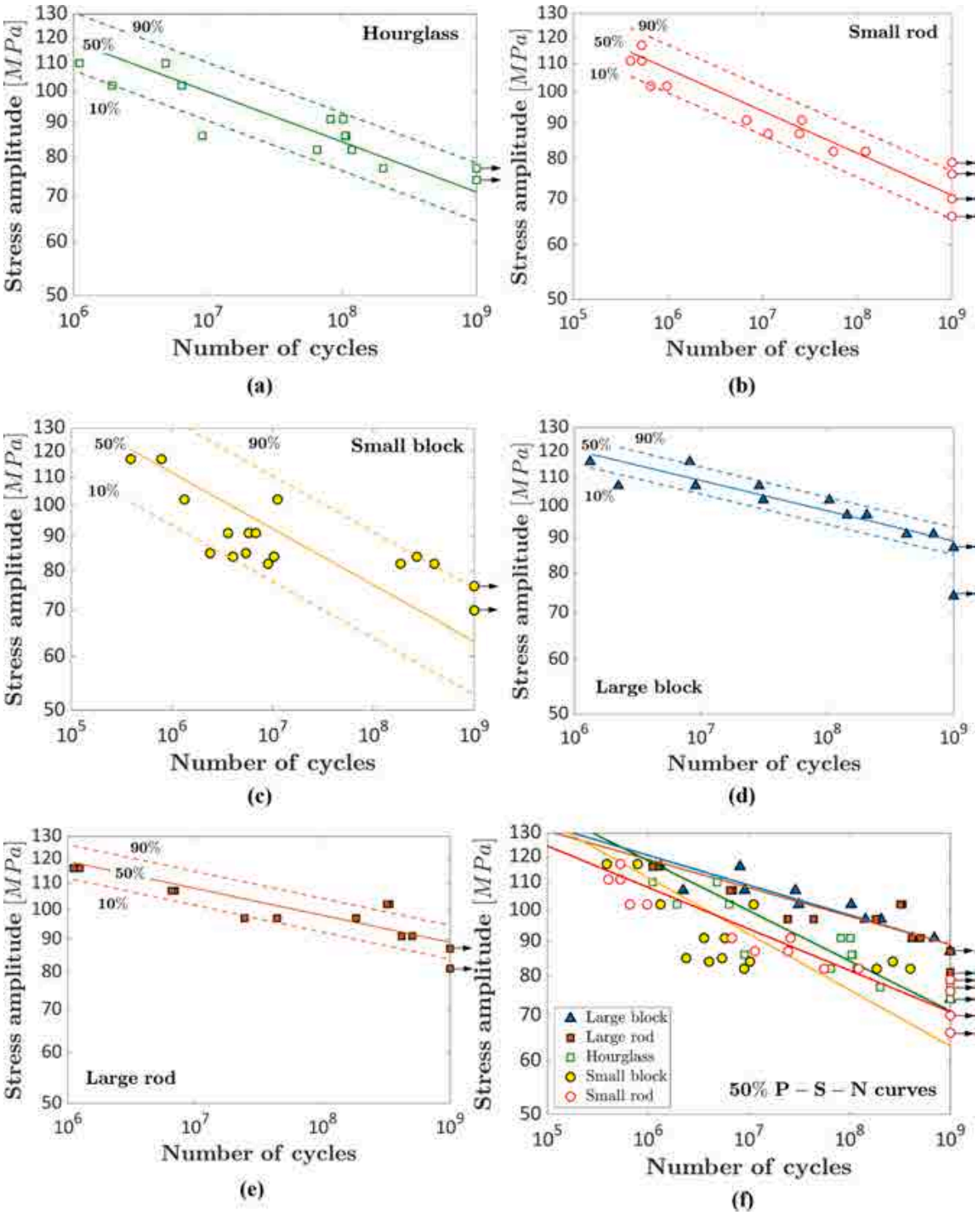

Fig. 12. Estimated P-S-N curves for (a) HG (b) SR (c) SB (d) LB (e) LR and (f) all investigated geometries.

and entrapped gas pores was the parameter of max. axis (i.e. defect size) while sphericity was found to be significantly less useful because both entrapped gas pores and KHs are spherical, with the latter being less so despite its significantly larger size. Hence, they suggested that to differentiate between these two sorts of defects, an obvious limit on defect size, such as 30 μm, might be useful. Significant sphericity overlaps were also detected between LoFs and KHs, as well as between entrapped gas pores and LoFs. This is mainly because of extremely small LoFs (defect size 10–20 μm) and their relatively high sphericity. The reported sphericity range for LoFs, KHs, and entrapped gas pores was between 0.5 and 0.9, 0.7–0.9, and 0.8–1.0, respectively and the sphericity value of 1.0 was only observed for entrapped gas pores [55]. That is why an additional defect analysis was conducted on the X-ray CT results in our work to separate defects with a sphericity value of 1.0 (i.e., fully spherical defects) and generate new histograms for these separated defects, as shown in Fig. 16(a–e) for HG, SR, SB, LB, and LR specimens, respectively.

As mentioned above, there was a simple limit of defect size at 30 μm between entrapped gas pores and KHs and significant overlaps in sphericity between entrapped gas pores and LoFs in the defect size range

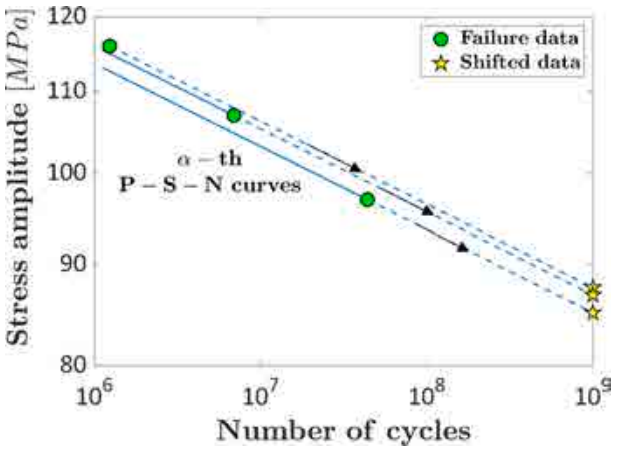

Fig. 13. Procedure for shifting the experimental failures at the reference number of cycles, N_{ref}, equal to 10^9 cycles.

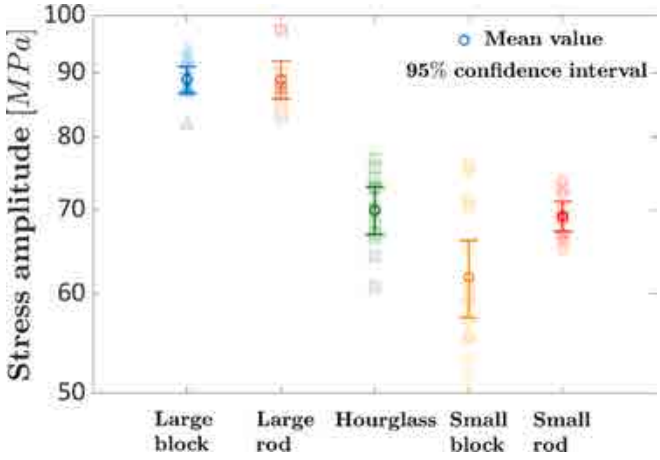

Fig. 14. Fatigue strength of the experimental failures shifted at 10^9 cycles.

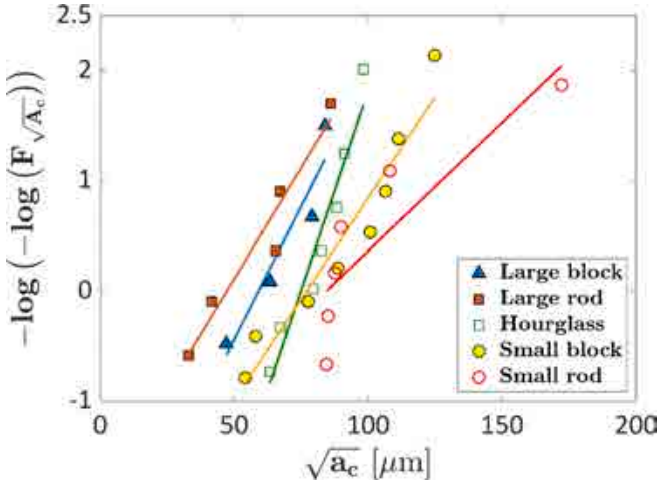

Fig. 15. Gumbel plot of the equivalent defect sizes for the investigated geometries and estimated LEVD functions.

of 10–20 μm [55]. Therefore, the defects in the histograms shown in Fig. 16, which are in the range of 20–30 μm, can be considered as the most potential representative of entrapped gas pores in this work since they are spherical. It can be seen from Fig. 16 that HG showed the highest amount of fully spherical defects, in both defect size ranges of 20–25 μm and 25–30 μm, compared to other samples. This may illustrate the increased number of entrapped gas pores in HG, SR, and SB specimens, as well as the reduced number of entrapped gas pores in LB and LR specimens.

However, it was observed that entrapped gas pores were not the critical defects responsible for fatigue crack initiation in any of the failed samples, according to the fractography analysis. That is probably the reason why HG samples, despite having the lowest cross-sectional area and the highest amount of entrapped gas pores, showed better VHCF performance compared to SR and SB samples. Several studies have found that the lack of appropriate overlap between two nearby melt pools may lead to LoF defect [38,56,57]. These defects cannot be prevented only by ensuring that the melt pools are deep enough. It is noteworthy that the current d_o/t_L of HG, SR, and SB specimens shows that the overlap depth of the melt pool is likewise more than the layer thickness, and consequently, it is expected that the two neighboring tracks and the next layers should have sufficiently fused [56]. Nevertheless, any anomalies like insufficient energy input, inconsistent process parameters, poor powder quality, or contamination that occur throughout the manufacturing process might cause this ratio to approach or perhaps go below one, which can then lead to the creation of LoF defects in some areas of the part. The LoF defects are known by their uneven shape which arise because of inadequate overlap between nearby melt pools or layers. It was observed by Darvish et al. [58] that the amount of LoF defects will decrease by increasing melt pool depth and melt pool overlap depth. Here, we can also interpret that the increased melt pool depth and melt pool overlap depth observed for LR and LB specimens in Fig. 4 would result in a lower amount of LoF defects in LR and LB specimens compared to other specimens.

The deeper melt pool relative to the layer thickness, along with sufficient overlap between consecutive melt pools (indicated by larger melt pool overlap depth) in LR and LB specimens, as reported in Table 3 with parameters dp/t_L and d_o/t_L, may account for the reduced occurrence of LoF defects compared to SR and SB specimens. This observation, as depicted in Fig. 6 for defect sizes exceeding 80 μm, underscores the influence of these specific process characteristics on defect formation, where LR and LB samples showed lower amounts of defects larger than 80 μm compared to all other samples. Notably, the HG sample exhibits a lower number of defects larger than 80 μm in diameter compared to SR and SB, despite having the lowest cross-sectional area, as well as the minimum value of dp/t_L. The melt pool may deviate towards the side of the melt pool that has a smaller powder layer thickness due to the oriented heat flow that occurs inside the melt pool. This phenomenon arises due to the solidified material's higher thermal conductivity compared to the powder [59]. Perhaps this deflection of the melt pool is unlikely to exert a significant effect on the depth of the melt pool; nonetheless, it may lead to a decreased melt pool overlap depth and a drop in the d_o/t_L ratio to less than unity, which subsequently results in the creation of unanticipated LoF defects in some location of the part. Furthermore, the probability of non-uniformity in the powder distribution may increase for parts with a larger surface area. This is because there is a greater likelihood of scraping, which might result in the disruption of the powder layer during the powder distribution process. This could serve as another explanation for why the HG specimens exhibited a reduced occurrence of larger-sized defects. The maximum defect size observed for the HG specimen from the XCT scan (108 μm) was bigger than LR (97 μm), LB (100 μm), and almost equal to SR (107 μm) and much smaller than SB (121 μm). This observation aligns with the VHCF data presented in Fig. 8, where LR and LB specimens demonstrated the highest fatigue performance, succeeded by HG, SR, and SB specimens. This hierarchy is logical since larger defects are typically more detrimental under cyclic loading, and they are often associated with shorter fatigue lives [10,60–63]. It is worth stating that the sphericity values of the largest defects were 0.55, 0.58, 0.86, 0.60, and 0.58 for HG, SR, SB, LB, and LR, respectively. This also aligns with the range of sphericity observed for LoF defects which was between 0.5 and 0.9 in [55].

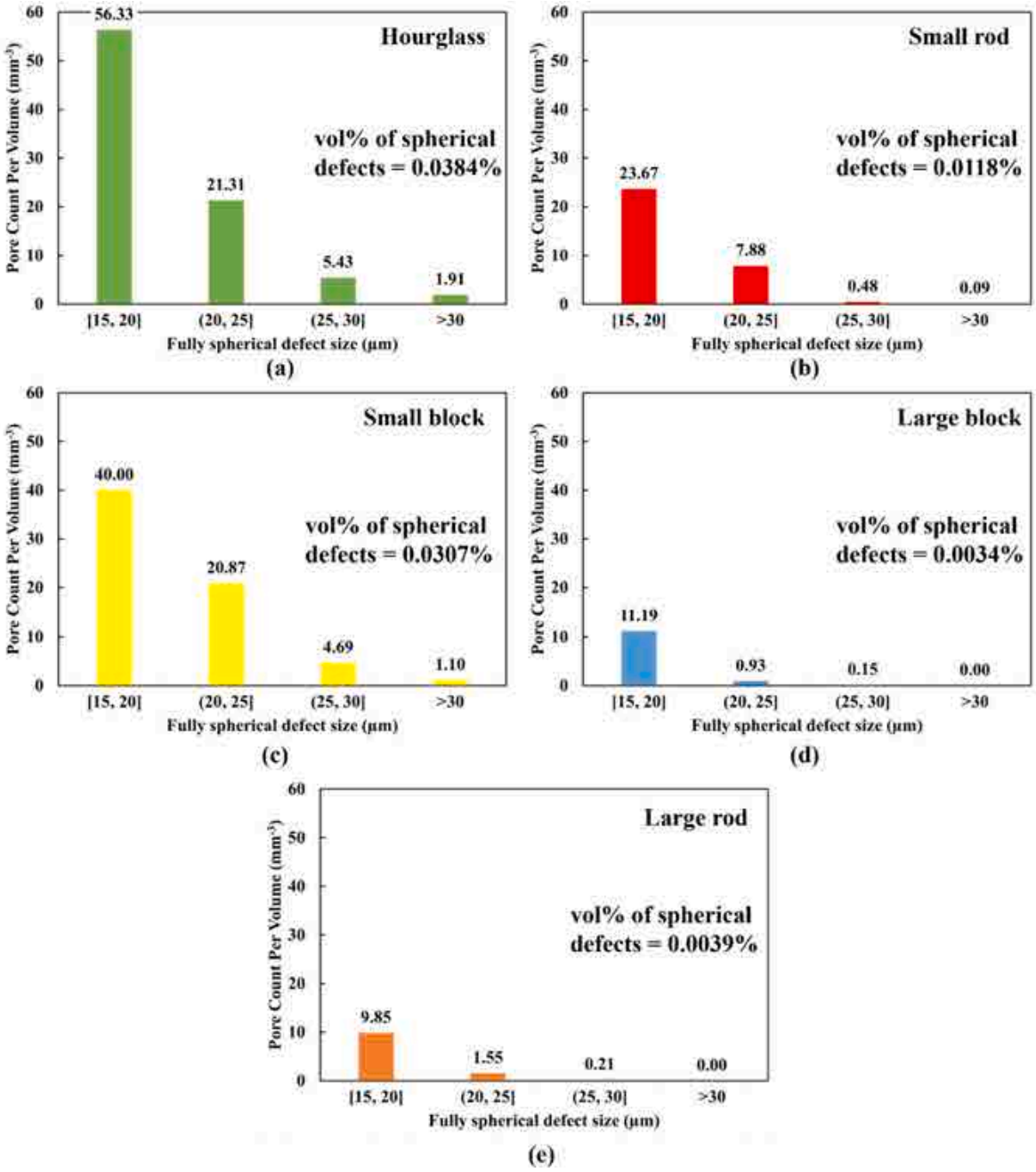

Fig. 16. X-ray CT results show the defect distribution of fully spherical porosities (i.e., defects with sphericity value of 1.0) for (a) HG (b) SR (c) SB (d) LB (e) LR.

Furthermore, it was discovered from fractography analysis that the location of the critical defect had the most important influence factor on the VHCF response of LB-PBF AlSi10Mg specimens, and the crack initiation position of HG, SR, and SB (i.e., group of specimens with the smaller cross-sectional area) under VHCF was closer to the edge of equivalent fracture surface, whereas the cases of LB and LR (i.e., group of specimens with larger cross-sectional area) were more likely to feature subsurface and internal crack initiation sites with fisheye patterns, according to the fractography data provided in Table 6. This was also observed in [28], where Tridello et al. found that critical defects were concentrated close to the surface in vertically built Hourglass specimens (specimens with smaller cross-sectional area) while for vertically built Gaussian specimens (specimens with larger cross-sectional area) some critical defects were farther from the surface (up to 1.5 mm from the surface). This could be due to the differences in distance from the free printing surface. As depicted in Fig. 2(a), the gage section of final ultrasonic fatigue samples obtained from larger parts (LR and LB) had a larger distance with the outer surface of the part during printing compared to the fatigue samples obtained from smaller parts (HG, SR and SB).

Another possible factor that we should consider for explaining the effect of part geometry on the fatigue performance of LB-PBF AlSi10Mg could be residual stress distribution. The applied stress relieve heat treatment in this study potentially reduces the detrimental residual stress in general and the residual stress distribution is further related to the size of the specimens. Thus, specimens with various geometries face different residual stress distributions after stress relieve heat treatment. By lowering the thermal gradients and cooling rates during the LB-PBF process, residual stress is mitigated by a significant degree by reducing the mismatch in thermal strains [64]. This may show that the bigger parts (LR and LB) had lower residual stress since they experienced a lower cooling rate during AM as was explained in section 4.3, and this

would cause a better fatigue performance compared to smaller parts.

This research indicates that a complete knowledge of the impacts of part geometry and size on the ensuing thermal history is essential for the effective establishment of specimen property to part performance correlations. These effects can have a significant impact on the distribution of defects and, as a result, the fatigue lives of LB-PBF parts especially in the VHCF regime. Establishing property-performance relationships for LB-PBF parts in the VHCF domain may be also achieved by modifying process parameters as it was obtained for the HCF regime in [31] to ensure resemblance in the thermal histories of the part's crucial region and the test samples.

5. Conclusion

The current investigation quantified the influence of part geometry and dimensions on both defect distribution and melt pool dimensions and subsequently examined how these factors govern the very high cycle fatigue (VHCF) response of AlSi10Mg components produced via laser beam powder bed fusion (LB-PBF) technique. The presence, size, and positioning of lack of fusion (LoF) defects, serving as initiation sites for cracks, were correlated with variations in fatigue lifetimes within the VHCF regime. The microstructural evaluation was conducted to discern alterations in melt pool dimensions and overlap depth, serving as indicators of the thermal history experienced during the LB-PBF process. It was recognized that the formation and distribution of these defects are influenced by the thermal profile encountered during laser-based fabrication. The following conclusions are drawn:

1. Microstructural analysis revealed that the hourglass-shaped specimen exhibited the lowest average melt pool depth in contrast to the large block and large rod specimens, which demonstrated deeper melt pools.
2. X-ray CT porosity analysis showed that small rod specimens had the highest total amount of defects which was followed by a small block, hourglass, large block, and large rod, respectively.
3. The large rod and large block specimens, characterized by fewer and smaller defects, demonstrated the highest fatigue strength. Conversely, the hourglass specimens, with intermediate defect characteristics, exhibited a slightly lower fatigue strength, and the small block and small rod specimens, harboring the highest quantity and larger-sized defects, displayed the shortest fatigue lives among the tested specimens.
4. The increased melt pool depth and especially melt pool overlap depth observed for large rod and large block specimens resulted in the lower amount and smaller size of irregular shape LoF defects in these specimens compared to other specimens. This can explain why large rod and large block samples showed much better fatigue performance in the VHCF regime.
5. The data obtained from statistical analyses further validated that the part geometry effect is relevant and affects the fatigue strength in the VHCF life region.

This study highlighted that the fatigue response is significantly influenced by the distance from the free printing surface. Specimens obtained from larger parts, regardless of their shape (rod or block), exhibited much better VHCF response and less variability compared to specimens obtained from small parts (small block and small box) and hourglass parts. It was observed that even just a small alteration in the size or shape of a part made with LB-PBF may have a considerable impact on the formation and distribution of defects. These defects ultimately determine the overall strength and durability of the part when subjected to cyclic loading. There is a notable concern regarding the correlation and utilization of characteristics achieved from small laboratory samples or witness coupons to evaluate the performance of parts in fatigue-sensitive applications. Hence, more research is required to achieve a better comprehension of property-performance relationships, it is crucial to consider how they are influenced by process-structure interrelationships. Furthermore, it is necessary to establish a methodology for designing test specimens that accurately reflect the most crucial area of the part subjected to operational cyclic loading. These investigations are essential for establishing uniformity, assessing quality, and verifying the suitability of LB-PBF parts for safety–critical purposes.

CRediT authorship contribution statement

Kamin Tahmasbi: Writing – original draft, Methodology, Investigation, Formal analysis. **Muztahid Muhammad:** Writing – original draft, Methodology, Data curation. **Maryam Avateffazeli:** Methodology, Investigation. **Mohammadreza Yaghoobi:** Writing – review & editing, Validation, Investigation, Formal analysis. **Andrea Tridello:** Writing – review & editing, Software, Methodology, Data curation. **Davide S. Paolino:** Writing – review & editing, Validation, Resources, Investigation. **Shuai Shao:** Writing – review & editing, Validation, Data curation. **Nima Shamsaei:** Writing – review & editing, Validation, Resources, Investigation, Conceptualization. **Meysam Haghshenas:** Supervision, Resources, Project administration, Funding acquisition, Conceptualization.

Declaration of competing interest

The authors declare that they have no known competing financial interests or personal relationships that could have appeared to influence the work reported in this paper.

Data availability

Data will be made available on request.

Appendix A:. Summary of the ultrasonic fatigue data of LB-PBF AlSi10Mg

Table A1
Fatigue test results of LB-PBF AlSi10Mg subjected to ultrasonic fatigue testing at 20 kHz.

Specimen type	Specimen ID	Stress amplitude, σ_a (MPa)	Number of cycles to failure, N_f
	HG1	74	>1.00E+09
	HG12	77	2.02E+08
	HG13	77	>1.00E+09
	HG6	82	1.18E+08
	HG9	82	6.50E+07
	HG10	86	1.07E+08

(*continued on next page*)

Table A1 (*continued*)

Specimen type	Specimen ID	Stress amplitude, σ_a (MPa)	Number of cycles to failure, N_f
	HG11	86	9.08E+06
Hourglass	HG15	86	1.05E+08
	HG3	91	1.02E+08
	HG17	91	8.19E+07
	HG7	102	6.39E+06
	HG8	102	1.94E+06
	HG2	110	1.11E+06
	HG14	110	4.85E+06
	SR1	66	>1.00E+09
	SR7	70	>1.00E+09
	SR3	76	>1.00E+09
	SR16	79	>1.00E+09
Small rod	SR8	82	1.23E+08
	SR14	82	5.60E+07
	SR9	87	1.15E+07
	SR15	87	2.46E+07
	SR13	91	6.80E+06
	SR17	91	2.60E+07
	SR5	102	6.60E+05
	SR10	102	9.80E+05
	SR11	111	4.04E+05
	SR12	111	5.32E+05
	SR19	117	5.32E+05
	SB1	70	>1.00E+09
	SB2	76	>1.00E+09
	SB4	82	9.01E+06
	SB5	82	1.86E+08
	SB12	82	4.02E+08
	SB9	84	4.03E+06
	SB10	84	2.69E+08
	SB11	84	1.03E+07
Small block	SB15	85	2.39E+06
	SB16	85	5.43E+06
	SB3	91	5.78E+06
	SB8	91	6.80E+06
	SB14	91	3.60E+06
	SB18	102	1.33E+06
	SB19	102	1.12E+07
	SB6	116	7.88E+05
	SB7	116	3.90E+05
	LB1	74	>1.00E+09
	LB2	87	>1.00E+09
	LB9	91	6.94E+08
	LB10	91	4.24E+08
	LB7	97	1.44E+08
	LB11	97	2.06E+08
Large block	LB14	102	1.04E+08
	LB15	102	3.13E+07
	LB5	107	2.90E+07
	LB6	107	2.23E+06
	LB12	107	9.11E+06
	LB3	116	8.18E+06
	LB4	116	1.33E+06
	LR12	81	>1.00E+09
	LR2	87	>1.00E+09
	LR9	91	4.18E+08
	LR11	91	5.05E+08
	LR5	97	4.40E+07
	LR6	97	1.83E+08
Large rod	LR16	97	2.44E+07
	LR14	102	3.35E+08
	LR15	102	3.20E+08
	LR4	107	6.93E+06
	LR10	107	6.55E+06
	LR3	116	1.24E+06
	LR13	116	1.11E+06

References

[1] Tusher MMH, Ince A. A systematic review on high cycle and very high cycle fatigue behavior of laser powder bed fused (L-PBF) Al-Si alloys. Eng Fail Anal 2023:107667.
[2] Raja A, Cheethirala SR, Gupta P, Vasa NJ, Jayaganthan R. A review on the fatigue behaviour of AlSi10Mg alloy fabricated using laser powder bed fusion technique. J Mater Res Technol 2022;17:1013–29.
[3] Tridello A, Fiocchi J, Biffi CA, Chiandussi G, Rossetto M, Tuissi A, et al. Effect of microstructure, residual stresses and building orientation on the fatigue response up to 109 cycles of an SLM AlSi10Mg alloy. Int J Fatigue 2020;137:105659.
[4] Rao H, Giet S, Yang K, Wu X, Davies CHJ. The influence of processing parameters on aluminium alloy A357 manufactured by Selective Laser Melting. Mater Des 2016;109:334–46.
[5] Jian ZM, Qian GA, Paolino DS, Tridello A, Berto F, Hong YS. Crack initiation behavior and fatigue performance up to very-high-cycle regime of AlSi10Mg fabricated by selective laser melting with two powder sizes. Int J Fatigue 2021;143:106013.
[6] Andani MT, Dehghani R, Karamooz-Ravari MR, Mirzaeifar R, Ni J. A study on the effect of energy input on spatter particles creation during selective laser melting process. Addit Manuf 2018;20:33–43.
[7] Rhein RK, Shi Q, Arjun Tekalur S, Wayne Jones J, Carroll JW. Effect of direct metal laser sintering build parameters on defects and ultrasonic fatigue performance of additively manufactured AlSi10Mg. Fatigue Fract Eng Mater Struct 2021;44(2):295–305.
[8] Ferro P, Fabrizi A, Berto F, Savio G, Meneghello R, Rosso S. Defects as a root cause of fatigue weakening of additively manufactured AlSi10Mg components. Theor Appl Fract Mech 2020;108:102611.
[9] Kan WH, Nadot Y, Foley M, Ridosz L, Proust G, Cairney JM. Factors that affect the properties of additively-manufactured AlSi10Mg: Porosity versus microstructure. Addit Manuf 2019;29:100805.
[10] Muhammad M, Nezhadfar PD, Thompson S, Saharan A, Phan N, Shamsaei N. A comparative investigation on the microstructure and mechanical properties of additively manufactured aluminum alloys. Int J Fatigue 2021;146:106165.
[11] Piette TD, Warren RJ, Spangenberger AG, Hummelt EJ, Lados DA. Microstructure evolution, fatigue crack growth, and ultrasonic fatigue in As-fabricated laser powder bed and conventionally cast Al–10Si-0.4 Mg: A mechanistic understanding and integrated flaw-sensitive fatigue design methods. Mater Sci Eng A 2021;825:141892.
[12] Xu Z, Liu A, Wang X. Fatigue performance and crack propagation behavior of selective laser melted AlSi10Mg in 0, 15, 45 and 90 building directions. Mater Sci Eng A 2021;812:141141.
[13] Xu ZW, Wang Q, Wang XS, Tan CH, Guo MH, Gao PB. High cycle fatigue performance of AlSi10mg alloy produced by selective laser melting. Mech Mater 2020;148:103499.
[14] Qian G, Jian Z, Qian Y, Pan X, Ma X, Hong Y. Very-high-cycle fatigue behavior of AlSi10Mg manufactured by selective laser melting: Effect of build orientation and mean stress. Int J Fatigue 2020;138:105696.
[15] Beretta S, Gargourimotlagh M, Foletti S, Du Plessis A, Riccio M. Fatigue strength assessment of "as built" AlSi10Mg manufactured by SLM with different build orientations. Int J Fatigue 2020;139:105737.
[16] Zhang Y, Li X, Yuan S, Sun R, Sakai T, Lashari MI, et al. High-cycle-fatigue properties of selective-laser-melted AlSi10Mg with multiple building directions. Int J Mech Sci 2022;224:107336.
[17] Awd M, Stern F, Kampmann A, Kotzem D, Tenkamp J, Walther F. Microstructural characterization of the anisotropy and cyclic deformation behavior of selective laser melted AlSi10Mg structures. Metals 2018;8(10):825.
[18] Wu H, Li J, Wei Z, Wei P. Effect of processing parameters on forming defects during selective laser melting of AlSi10Mg powder. Rapid Prototyp J 2020;26(5):871–9.
[19] Lu X, Yang X, Zhao X, Yang H, Li MV. Additively manufactured AlSi10Mg ultrathin walls: Microstructure and nano-mechanical properties under different energy densities and interlayer cooling times. Mater Sci Eng A 2022;835:142652.
[20] Limbasiya N, Jain A, Soni H, Wankhede V, Krolczyk G, Sahlot P. A comprehensive review on the effect of process parameters and post-process treatments on microstructure and mechanical properties of selective laser melting of AlSi10Mg. J Mater Res Technol 2022;21:1141–76.
[21] Wu Z, Wu S, Bao J, Qian W, Karabal S, Sun W, et al. The effect of defect population on the anisotropic fatigue resistance of AlSi10Mg alloy fabricated by laser powder bed fusion. Int J Fatigue 2021;151:106317.
[22] Chmelko V, Šulko M, Škriniarová J, Margetin M, Gašparík M, Košťo T, et al. Strength and cyclic properties of additive vs conventionally produced material AlSi10Mg. Materials 2023;16(7):2598.
[23] Gerov MV, Vladislavskaya EY, Terent'ev VF, Prosvirnin DV, Antonova OS, Kolmakov AG. Fatigue strength of an AlSi10Mg alloy fabricated by selective laser melting. Russian Metallurgy (Metally) 2019;2019:392–7.
[24] Pegues J, Roach M, Williamson RS, Shamsaei N. Surface roughness effects on the fatigue strength of additively manufactured Ti-6Al-4V. Int J Fatigue 2018;116:543–52.
[25] Zheng B, Zhou Y, Smugeresky JE, Schoenung JM, Lavernia EJ. Thermal behavior and microstructural evolution during laser deposition with laser-engineered net shaping: Part I Numerical calculations. Metall Mater Trans A 2008;39(9):2228–36.
[26] Costa L, Vilar R, Reti T, Deus AM. Rapid tooling by laser powder deposition: Process simulation using finite element analysis. Acta Mater 2005;53(14):3987–99.
[27] Mahmoudi M, Elwany A, Yadollahi A, Thompson SM, Bian L, Shamsaei N. Mechanical properties and microstructural characterization of selective laser melted 17–4 PH stainless steel. Rapid Prototyp J 2017.
[28] Tridello A, Fiocchi J, Biffi CA, Rossetto M, Tuissi A, Paolino DS. Size-effects affecting the fatigue response up to 10^9 cycles (VHCF) of SLM AlSi10Mg specimens produced in horizontal and vertical directions. Int J Fatigue 2022;160:106825.
[29] Paolino DS, Tridello A, Fiocchi J, Biffi CA, Chiandussi G, Rossetto M, et al. VHCF response up to 109 cycles of SLM AlSi10Mg specimens built in a vertical direction. Appl Sci 2019;9(15):2954.
[30] Shrestha R, Shamsaei N, Seifi M, Phan N. An investigation into specimen property to part performance relationships for laser beam powder bed fusion additive manufacturing. Addit Manuf 2019;29:100807.
[31] Soltani-Tehrani A, Shrestha R, Phan N, Seifi M, Shamsaei N. Establishing specimen property to part performance relationships for laser beam powder bed fusion additive manufacturing. Int J Fatigue 2021;151:106384.
[32] Shanbhag G, Wheat E, Moylan S, Vlasea M. Effect of specimen geometry and orientation on tensile properties of Ti-6Al-4V manufactured by electron beam powder bed fusion. Addit Manuf 2021;48:102366.
[33] Zhao L, Song L, Macías JGS, Zhu Y, Huang M, Simar A, et al. Review on the correlation between microstructure and mechanical performance for laser powder bed fusion AlSi10Mg. Addit Manuf 2022;56:102914.
[34] Shakil SI, Hadadzadeh A, Pirgazi H, Mohammadi M, Haghshenas M. Indentation-derived creep response of cast and laser powder bed fused AlSi10Mg alloy: air temperature. Micron 2021;103145.
[35] Nezhadfar PD, Shrestha R, Phan N, Shamsaei N. Fatigue behavior of additively manufactured 17–4 PH stainless steel: Synergistic effects of surface roughness and heat treatment. Int J Fatigue 2019;124:188–204.
[36] Ultrasonic Fatigue Testing System, Shimadzu USF-2000A.
[37] ASTM E8/E8M-16a (2016) Standard Test Methods for Tension Testing of Metallic Materials. ASTM International, West Conshohocken.
[38] Specification for control and qualification of laser powder bed fusion metallurgical processes, MSFC Technical Standard MSFC-SPEC-3717 (2017).
[39] Alghamdi F, Song X, Hadadzadeh A, Shalchi-Amirkhiz B, Mohammadi M, Haghshenas M. Post heat treatment of additive manufactured AlSi10Mg: On silicon morphology, texture and small-scale properties. Mater Sci Eng A 2020;783:139296.
[40] Alghamdi F, Haghshenas M. Microstructural and small-scale characterization of additive manufactured AlSi10Mg alloy. SN Appl Sci 2019;1(255).
[41] Shakil SI, Hadadzadeh A, Shalchi Amirkhiz B, Pirgazi H, Mohammadi M, Haghshenas M. Additive manufactured versus cast AlSi10Mg alloy: Microstructure and micromechanic. Results in Materials 2021;10:100178.
[42] Tridello A, Fiocchi J, Biffi CA, Chiandussi G, Rossetto M, Tuissi A, et al. Influence of the annealing and defects on the VHCF behavior of an SLM AlSi10Mg alloy. Fatigue Fract Eng Mater Struct 2019;42(12):2794–807.
[43] Campbell FC. Fatigue and fracture: understanding the basics. ASM Int 2012.
[44] Murakami Y. Metal fatigue: effects of small defects and nonmetallic inclusions. Academic Press 2019.
[45] Yamashita Y, Murakami T, Mihara R, Okada M, Murakami Y. Defect analysis and fatigue design basis for Ni-based superalloy 718 manufactured by additive manufacturing. Procedia Struct Integrity 2017;7:11–8.
[46] Masuo H, Tanaka Y, Morokoshi S, Yagura H, Uchida T, Yamamoto Y, et al. Influence of defects, surface roughness and HIP on the fatigue strength of Ti-6Al-4V manufactured by additive manufacturing. Int J Fatigue 2018;117:163–79.
[47] Uzan NE, Shneck R, Yeheskel O, Frage N. Fatigue of AlSi10Mg specimens fabricated by additive manufacturing selective laser melting AM-SLM. Mater Sci Eng A 2017;704:229–37.
[48] Avateffazeli M, Webster G, Tahmasbi K, Haghshenas M. Very high cycle fatigue at elevated temperatures: A review on high temperature ultrasonic fatigue. J Space Safety Eng 2022.
[49] Behvar A, Sojoodi M, Elahinia M, Niutta CB, Tridello A, Paolino DS, et al. Very high cycle fatigue of fiber-reinforced polymer composites: Uniaxial ultrasonic fatigue. Fatigue Fract Eng Mater Struct 2024.
[50] Tahmasbi K, Alharthi F, Webster G, Haghshenas M. Dynamic frequency-dependent fatigue damage in metals: A state-of-the-art review. Forces Mech 2023;10:100167.
[51] Halperin M, Hartley HO, Hoel PG. Recommended standards for statistical symbols and notation: copss committee on symbols and notation. Am Stat 1965;19(3):12–4.
[52] Yang KV, Rometsch P, Jarvis T, Rao J, Cao S, Davies C, et al. Porosity formation mechanisms and fatigue response in Al-Si-Mg alloys made by selective laser melting. Mater Sci Eng A 2018;712:166–74.
[53] Sun Z, Tan X, Tor SB, Chua CK. Simultaneously enhanced strength and ductility for 3D-printed stainless steel 316L by selective laser melting. NPG Asia Mater 2018;10(4):127–36.
[54] Malekipour E, El-Mounayri H. Common defects and contributing parameters in powder bed fusion AM process and their classification for online monitoring and control: a review. Int J Adv Manuf Technol 2018;95:527–50.
[55] Poudel A, Yasin MS, Ye J, Liu J, Vinel A, Shao S, et al. Feature-based volumetric defect classification in metal additive manufacturing. Nat Commun 2022;13(1):6369.
[56] Cunningham R, Narra SP, Montgomery C, Beuth J, Rollett AD. Synchrotron-based X-ray microtomography characterization of the effect of processing variables on porosity formation in laser power-bed additive manufacturing of Ti-6Al-4V. JOM 2017;69:479–84.
[57] Tang M, Pistorius PC, Beuth JL. Prediction of lack-of-fusion porosity for powder bed fusion. Addit Manuf 2017;14:39–48.
[58] Darvish K, Chen ZW, Pasang T. Reducing lack of fusion during selective laser melting of CoCrMo alloy: Effect of laser power on geometrical features of tracks. Mater Des 2016;112:357–66.

[59] Dai D, Gu D. Tailoring surface quality through mass and momentum transfer modeling using a volume of fluid method in selective laser melting of TiC/AlSi10Mg powder. Int J Mach Tool Manu 2015;88:95–107.
[60] Shi T, Sun J, Li J, Qian G, Hong Y. Machine learning based very-high-cycle fatigue life prediction of AlSi10Mg alloy fabricated by selective laser melting. Int J Fatigue 2023;171:107585.
[61] Romano S, Brückner-Foit A, Brandão A, Gumpinger J, Ghidini T, Beretta S. Fatigue properties of AlSi10Mg obtained by additive manufacturing: Defect-based modelling and prediction of fatigue strength. Eng Fract Mech 2018;187:165–89.
[62] Ngnekou JND, Nadot Y, Henaff G, Nicolai J, Kan WH, Cairney JM, et al. Fatigue properties of AlSi10Mg produced by additive layer manufacturing. Int J Fatigue 2019;119:160–72.
[63] Beevers E, Brandão AD, Gumpinger J, Gschweitl M, Seyfert C, Hofbauer P, et al. Fatigue properties and material characteristics of additively manufactured AlSi10Mg–Effect of the contour parameter on the microstructure, density, residual stress, roughness and mechanical properties. Int J Fatigue 2018;117:148–62.
[64] Bartlett JL, Li X. An overview of residual stresses in metal powder bed fusion. Addit Manuf 2019;27:131–49.